crystals

MDPI

Review

Assembly of Multi-Dimensional Microstructures of MXene towards Wearable Electromagnetic Attenuating Devices

Min Zhang [1,*] and Mao-Sheng Cao [2,*]

[1] Department of Physics, Beijing Technology and Business University, Beijing 100048, China
[2] School of Materials Science and Engineering, Beijing Institute of Technology, Beijing 100081, China
* Correspondence: zhangm@btbu.edu.cn (M.Z.); caomaosheng@bit.edu.cn (M.-S.C.)

Abstract: MXene is a competitive and attractive 2D material used in wearable electromagnetic devices due to its laminated nanostructure, abundant surface terminations and high conductivity. Assembling MXene nanosheets into multi-dimensional microstructures is considered to be an effective method for improving the overall performance of MXene-based composites, especially their electromagnetic attenuation and wearability performance. This article focuses on the strategies for assembling multi-dimensional MXene microstructures, from 0D spheres and 1D fibers to 2D films and 3D architectures. The origin of the electromagnetic response of MXene microstructures is revealed, and the corresponding electromagnetic absorption and interference shielding performance are shown. Furthermore, additional extended functions that serve wearable electromagnetic attenuation devices are highlighted. Finally, the application prospects and challenges of wearable electromagnetic devices, as well as the function integration of multi-dimensional MXene composites, are summarized.

Keywords: MXenes; electromagnetic absorption; electromagnetic shielding; wearable electromagnetic attenuating devices; multifunctional application

check for updates

Citation: Zhang, M.; Cao, M.-S. Assembly of Multi-Dimensional Microstructures of MXene towards Wearable Electromagnetic Attenuating Devices. *Crystals* **2023**, *13*, 1612. https://doi.org/10.3390/cryst13121612

Academic Editors: Qui Thanh Hoai Ta and Ngo Tran

Received: 19 October 2023
Revised: 11 November 2023
Accepted: 16 November 2023
Published: 21 November 2023

Copyright: © 2023 by the authors. Licensee MDPI, Basel, Switzerland. This article is an open access article distributed under the terms and conditions of the Creative Commons Attribution (CC BY) license (https://creativecommons.org/licenses/by/4.0/).

1. Introduction

With a significant increase in the number of wireless communication devices, the security of communication without electromagnetic interference and the prevention of human overexposure to electromagnetic radiation are key requirements [1]. Communication equipment and humans, especially infants, pregnant women and workers, engaged in wireless communication need wearable electromagnetic attenuation devices, such as radiation-shielding clothing and shields, to attenuate the negative effects of electromagnetic waves. In addition to clothing, wearable electromagnetic attenuation devices are also integrated into portable electronic bracelets, smart watches and other communication devices. In addition, if military equipment is equipped with electromagnetic attenuation devices, the reflected waves can be reduced so that they are not detected by radars. A prerequisite for the realization of electromagnetic attenuation devices is to assemble electromagnetic attenuation materials into macroscopic films with good mechanical properties. The functional obtainment of an electromagnetic attenuation device is based on electromagnetic-absorbing materials or electromagnetic interference shielding materials, which can protect internal objects from radiation by absorbing or reflecting waves. In 2016, micron-scale MXene films were discovered to have superior electromagnetic shielding relative to metal/carbon materials due to their mechanical flexibility and metallic conductivity [2]. Since then, MXene, as a high-spirited horse, has immediately aroused exponential attention, and its performance can be switched from electromagnetic shielding to electromagnetic absorption by tailoring its microstructures and heterogeneous phases. Therefore, various MXene composites can fulfill the requirements of electromagnetic absorption or shielding for fabricating wearable devices.

The general formula of MXenes is $M_{n+1}X_nT_x$ (n = 1–3), with M denoting the early transition metal. X is the abbreviation for carbon and/or nitrogen and T_x denotes the surface

terminations of hydroxyl, oxygen or fluorine. The molecular structure of MXenes with $n = 2$ is shown at the center of Figure 1. The construction of multi-dimensional MXene composites, such as 0D spheres [3,4], 1D fibers [5,6], 2D films [7,8] and 3D architectures [9,10], will permit freedom in customizing the electromagnetic responses and mechanical properties of MXenes. Simultaneously, the diverse chemistry of the heterogeneous phases in MXene-based composites also assists MXene in tuning its physical and chemical properties [11]. Therefore, while electromagnetic properties are improved [12–14], MXene composites can achieve additional functions to facilitate their wearability, such as fatigue resistance [15], photothermal conversion [16], electrothermal conversion [17] and thermal management [18]. This multifunctional integration not only expands the application field of electromagnetic devices but also injects new vitality into the development of MXenes [19].

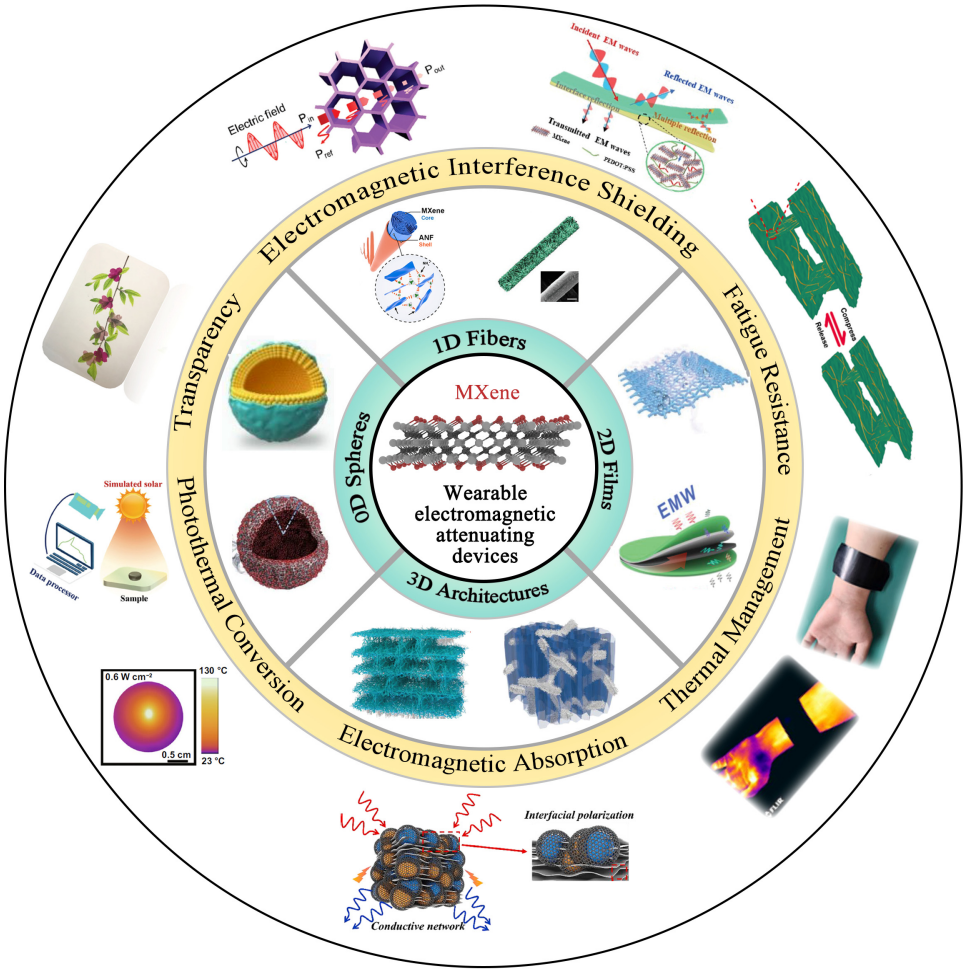


Figure 1. Schematic for multi-dimensional MXene microstructures and their applications: 0D spheres, reproduced from [3,4], with the permission of Royal Society of Chemistry and the authors, published by Springer Nature; 1D fibers, reproduced from [5,6], with the permission of Wiley-VCH and the authors, published by Springer Nature; 2D films, reproduced from [7,8], with the permission of Wiley-VCH and Royal Society of Chemistry; 3D architectures, reproduced from [9,10], with the permission of Royal Society of Chemistry and the authors, published by Wiley-VCH; electromagnetic responses, reproduced from [11–14], with the permission of Springer Nature, Elsevier and the authors, published by Wiley-VCH; fatigue resistance, reproduced from [15], with the permission of the American Chemical Society; photothermal conversion, reproduced from [16], with the permission of the authors, published by Springer Nature; electrothermal conversion, reproduced from [17], with the permission of Springer Nature; thermal management, reproduced from [18], with the permission of Springer Nature; transparent and printable, reproduced from [19], with the permission of Elsevier.

Herein, typical assembly strategies for multi-dimensional MXene structures are focused on. Electromagnetic attenuation mechanisms, including electromagnetic absorption and interference shielding, are emphasized, and the corresponding electromagnetic attenuating performance, reflection loss (RL) and shielding effectiveness (SE) of MXenes with different dimensions are illustrated. Then, we highlight several additional functions that are available for their integration into wearable electromagnetic attenuation devices.

2. Mechanism of Electromagnetic Attenuation

2.1. Electromagnetic Absorption

The microwave absorption performance of MXene composites is dominated by electromagnetic parameters. The absorbed electromagnetic energy is dissipated by dielectric loss and magnetic loss. Imaginary permittivity (ε'') and imaginary permeability (μ'') are parameters that characterize dielectric loss and magnetic loss. If MXene composites do not contain a magnetic phase, dielectric loss is the main source of loss. As shown in Figure 2a, dielectric loss consists of conduction loss (ε_c'') and polarization loss (ε_p'') [20]. For conduction loss, electromagnetic energy actuates electrons directionally within or among MXene nanosheets (Figure 2b,c) [21]. The long-range electrons transported among nanosheets play a crucial role in conduction loss [22]. This is attributed to the fact that contacting regions between the nanosheets have higher potential than the in-plane regions of the nanosheets. Thus, ε_c'' increases relative to the mass ratio and conductivity (Figure 2d). Polarization loss ε_p'' results from the inelastic polarization of dipoles and interfaces where relaxation occurs (Figure 2e) [23]. Dipole polarization relaxation is produced near the vacancy and cluster defects of MXene nanosheets, where charge distortion and electronic pinning effects result in the separation of positive and negative charge centers (Figure 2f) [24]. Interfacial polarization relaxation mainly appears in MXene composites [25–28]. Due to the different polarity and electrical properties of heterogeneous phases, the bound charges condensed at the interfaces are different, resulting in interface polarization, which can be described by the equivalent capacitor model. As shown in the inset of Figure 2g, the interface between the Ni shell and MXene core is circled by a dotted red box [29]. The corresponding charge density distribution in this region is shown in Figure 2f. The separate blue and yellow regions confirm the presence of interfacial polarization, whereas blue and yellow regions represent the accumulation of positive and negative charges, respectively. Therefore, MXenes with good electrical conductivity and abundant terminals can fulfill the requirements of high dielectric loss.

As the absence of an effective high-frequency magnetic response limits the tunable range of MXenes' electromagnetic properties, introducing a magnetic phase is an effective strategy for improving the impedance-matching property. Transition metals such as Fe, Co and Ni and their compounds are usually utilized as the magnetic component [30–32]. They will generate magnetic loss and promote the electromagnetic synergy effect [33].

Reflection loss (RL) is an indicator for evaluating microwave absorption performance, which is expressed as follows [34]:

$$\mathrm{RL(dB)} = 20\lg\frac{|Z_{in} - Z_0|}{|Z_{in} + Z_0|} \tag{1}$$

$$Z_{in} = Z_0\sqrt{\frac{\mu_r}{\varepsilon_r}}\tanh\left[j\frac{2\pi}{c}\sqrt{\varepsilon_r\mu_r}fd\right] \tag{2}$$

Z_{in} is the input impedance. Z_0 is the impedance of free space. ε_r, μ_r, c, f and d are the relative complex permittivity and permeability, light velocity, incident frequency and thickness, respectively. The criterion of effective electromagnetic absorption is an RL below −10 dB [35]. A particularly low RL value indicates excellent electromagnetic absorption. Obviously, the RL values are dominated by input impedance (Z_{in}) and Z_{in} is synergistically modulated by electromagnetic properties: ε_r and μ_r. When impedance is matched and the

impedance coefficient ($M_Z = 2Z_{in}'/(1 + |Z_{in}|^2)$) approaches 1, RL will reach the optimal value [36].

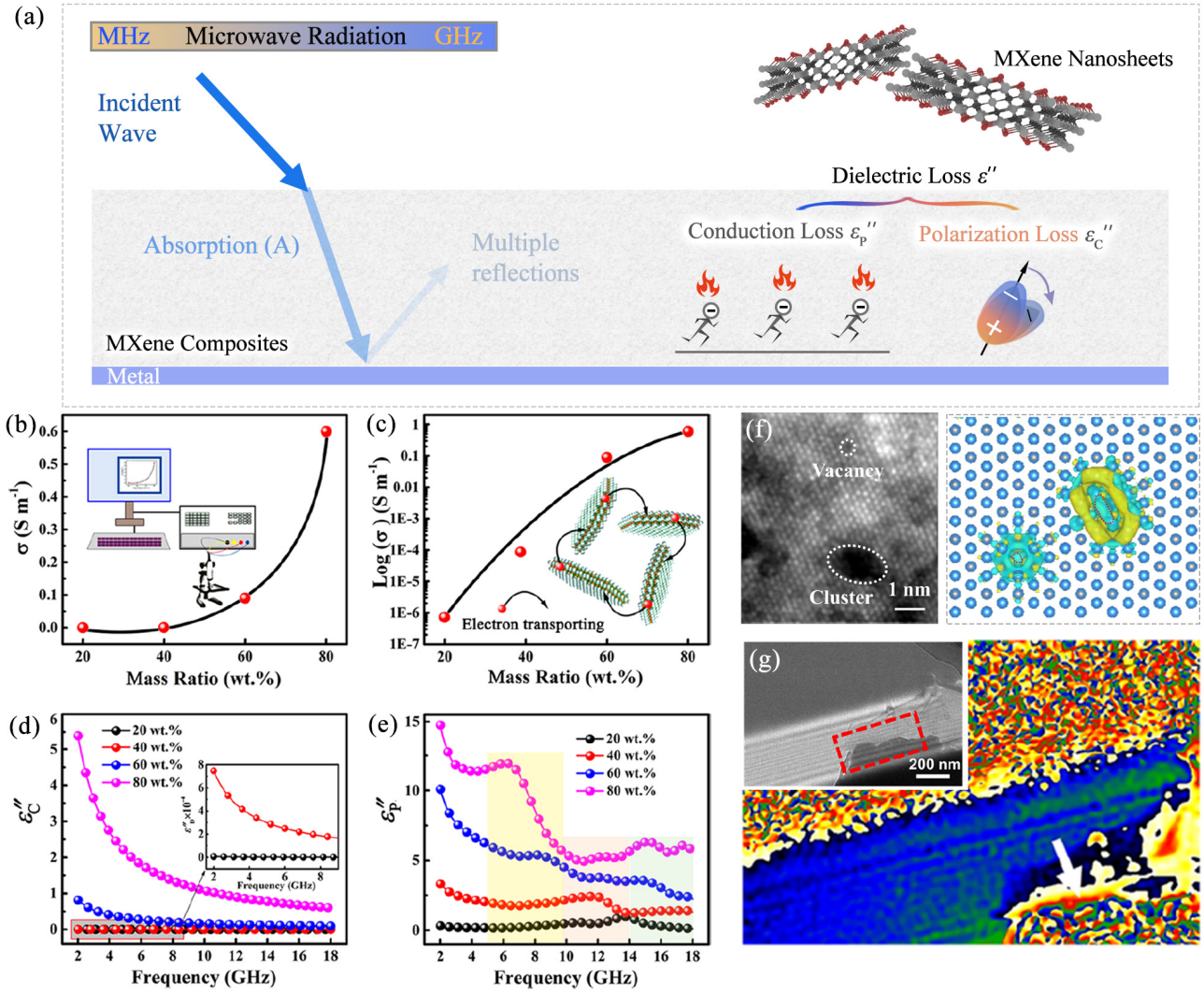


Figure 2. Electromagnetic absorption mechanism. (**a**) Schematic for the microwave absorption of MXenes. (**b**) Conductivity vs. mass ratio of MXene nanosheets. (**c**) Conductivity and schematic for electron transport. (**d**) Conduction loss of MXene composites. (**e**) Polarization loss of MXene composites; reproduced from [21], with the permission of the American Chemical Society. (**f**) Vacancies in MXene. The charge density distribution near vacancies; reproduced from [24], with the permission of Wiley-VCH. (**g**) Polarization charge density versus location. Inset, off-axis electron hologram; reproduced from [29], with the permission of the American Chemical Society.

2.2. Electromagnetic Interference Shielding

Shielding effectiveness (SE) is a parameter that characterizes the electromagnetic interference shielding performance. It is calculated based on the transmission, reflection and absorption coefficients (T, R and A). R and T are derived from the measured scattering parameters (S_{11} and S_{21}) as follows [37]:

$$R = |S_{11}|^2 \quad (3)$$

$$T = |S_{21}|^2 \quad (4)$$

Thus, A is represented by:

$$A = 1 - R - T \quad (5)$$

The total SE stands for the ability to shield the incident waves based on the reflection (SE_R) and absorption (SE_A) of a material. SE, SE_R and SE_A are expressed as follows [38]:

$$SE(dB) = 10 \times \lg(1/T) \quad (6)$$

$$SE_R(dB) = 10 \times \lg(1/(1-R)) \quad (7)$$

$$SE_A(dB) = 10 \times \lg((1-R)/T) \quad (8)$$

As shown in Figure 3a, the shielding performance reflects the proportion of transmitted electromagnetic waves, and a high SE value corresponds to low transmittance. Different from the RL value, reflection is crucial relative to a prominent SE value [39–41]. In general, reflection results from good conductivity and the mismatched impedance of the sample [42,43]. MXene has good electrical conductivity (Figure 3b), and the conductivity of the MXene composite is increased monotonically relative to an increase in the mass fraction of MXene [44,45]. Therefore, the corresponding electromagnetic interference shielding performance is improved due to the contribution of reflection (Figure 3c). Additionally, for materials with thicknesses that are less than the skin depth, multiple reflections should be considered [40,46]. As MXenes are obtained by etching MAX in acidic solutions, the remaining surface terminations of –OH, –H and –F facilitate MXenes to be processed in solutions via interface assembly, spinning, spraying, etc. At the same time, MXenes can bond to flexible substrates due to their functionalized surfaces. These advantages suggest that MXene is a candidate for wearable and flexible electromagnetic functional materials.

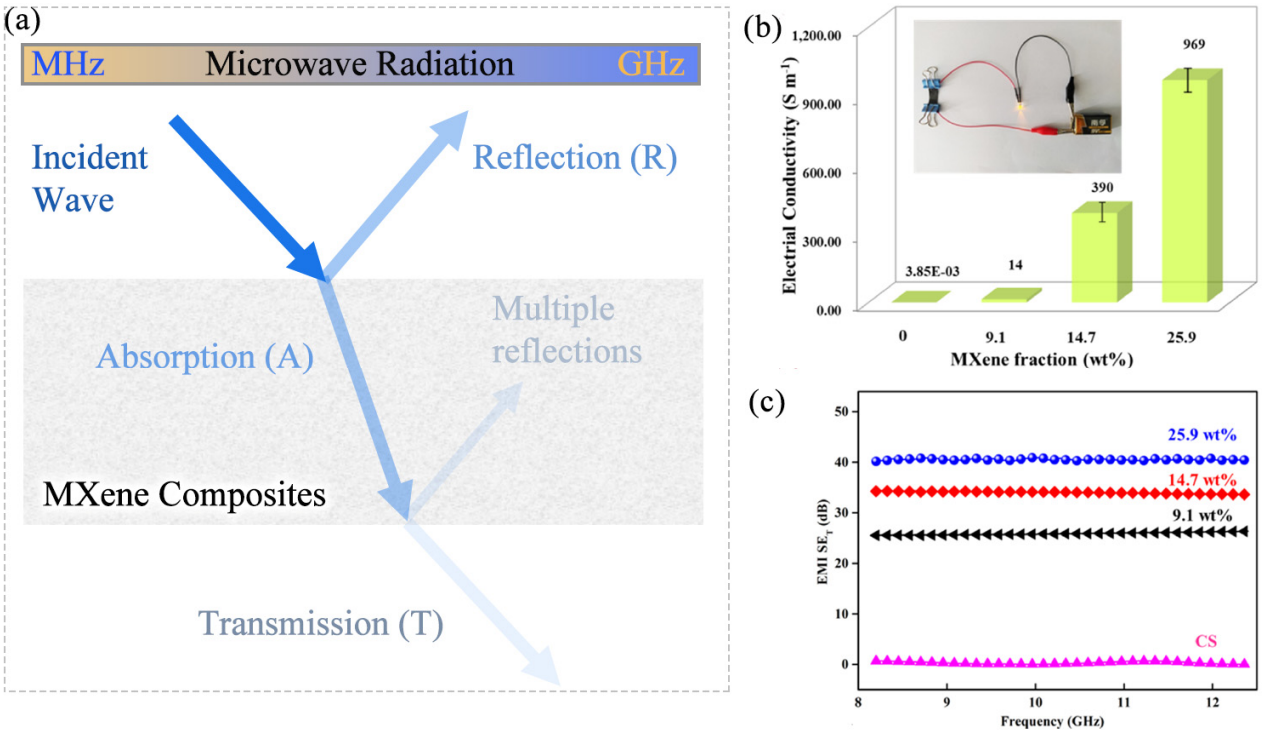


Figure 3. Electromagnetic interference shielding mechanism. (**a**) Schematic for the electromagnetic interference shielding of MXene composites. (**b**) Conductivity of chitosan/MXene films with different MXene fractions. (**c**) SE of chitosan and chitosan/MXene films with different MXene fractions; reproduced from [44], with the permission of Elsevier.

3. Assembly of Multi-Dimensional MXenes

An electromagnetic attenuation device requires not only excellent electromagnetic absorbing/shielding performance but also good mechanical properties in order to be wearable. Electromagnetic responses and attenuation performance can be effectively tuned by making MXenes with different dimensional structures. For 0D MXenes, the charges

are confined to the local 0D micron/nanometer region, and the limited conductivity is not conducive to conduction loss. Therefore, heterogeneous phases can be introduced to create interfaces that enhance the polarization relaxation loss. This facilitates the realization of high electromagnetic absorption rather than shielding. Obviously, 0D MXenes cannot be worn directly; secondary processing such as filtration or spraying is needed. A 1D MXene structure with a high aspect ratio can be knittable, and it is suitable for weaving fabrics and coverings. More importantly, woven 1D MXenes provide long-range transport channels for electrons, indicating that a strong conduction loss and reflection may occur. For 2D films and 3D architectures, especially aerogels and foams, their electromagnetic shielding performances are usually prominent due to the high conductivity caused by the interconnection of large areas of MXene nanosheets. When 2D/3D MXene structures reach the macroscopic scale, they can be worn directly. When a heterogeneous phase is introduced, the electromagnetic attenuation performance can be regulated, where electromagnetic absorption may appear.

Mechanical properties are the basis for judging whether electromagnetic attenuating materials can be worn for a long time, and these properties are dominated not only by the properties of material components but also by the sequential fabrication method. In this section, the fabrication techniques of 0D, 1D, 2D and 3D MXene structures are reviewed. In particular, the assembly strategies include 0D self-assembly driven by electrostatic attraction, hydrogen bonding and covalent bonding; 1D assembly methods relying on template materials and pinning; 2D assembly methods performed by Rayleigh–Benard convection, spraying and vacuum-assisted filtration; and 3D assembly methods with respect to in situ growth and freeze drying.

3.1. Zero-Dimensional Structures

As monodispersed MXene is a 2D nanosheet, the assembly of MXenes into other dimensions requires the support of template materials or external force from rigid molds. The interface assembly with the template material is mainly based on the interactions between atoms and molecules, such as electrostatic attraction, hydrogen bonding, covalent bonding and van der Waals action, which are the main assembly mechanisms. Generally, a template material with good mechanical properties not only jointly improves the wearability of composites but also introduces increased interfacial polarization.

3.1.1. Electrostatically Driven Self-Assembly

The surface terminations of –OH, –H and –F enable the negative charge of MXene [47]. This feature provides an opportunity for MXene nanosheets to be assembled into the structures of other dimensions via electrostatic attraction. Electrostatic assembly is performed when the concentration of MXene nanosheets is relatively low, where the positive core material attracts negative MXene nanosheets. For example, the zeta potential of $Ti_3C_2T_x$ is within the range of -25~-54 mV and the pH of 11.3–2.7. Thus, electrostatic attraction drives the assembly of $Ti_3C_2T_x$ nanosheets on the surface of positive polystyrene (PS) microspheres, constructing a 0D MXene-based sphere, as shown in Figure 4a [48]. When the concentration of MXene nanosheets increases and negative charges from $Ti_3C_2T_x$ are equal to the positive charges from PS microspheres, the electrostatic driving force disappears. If a template material lacks a positive surface and has no electrostatic attraction, surface modification is an option for endowing it with self-assembly capacities. Hong et al. functionalized the surface of $CoSe_2$ spheres via poly(diallyldimethylammonium chloride) (PDDA) [4]. After functionalization, the PDDA-$CoSe_2$ is positively charged, of which MXene nanosheets can be assembled on the surface (Figure 4b). Figure 4c shows that the thickness of the MXene shell is less than 5 nm. Overall, materials used as templates to generate electrostatic driving forces mainly include PS, PDDA, C_3N_4 and polyethyleneimine [49]. Because some materials can be removed via heat treatment or etching, suitable template materials can be employed to prepare hollow MXene microspheres.

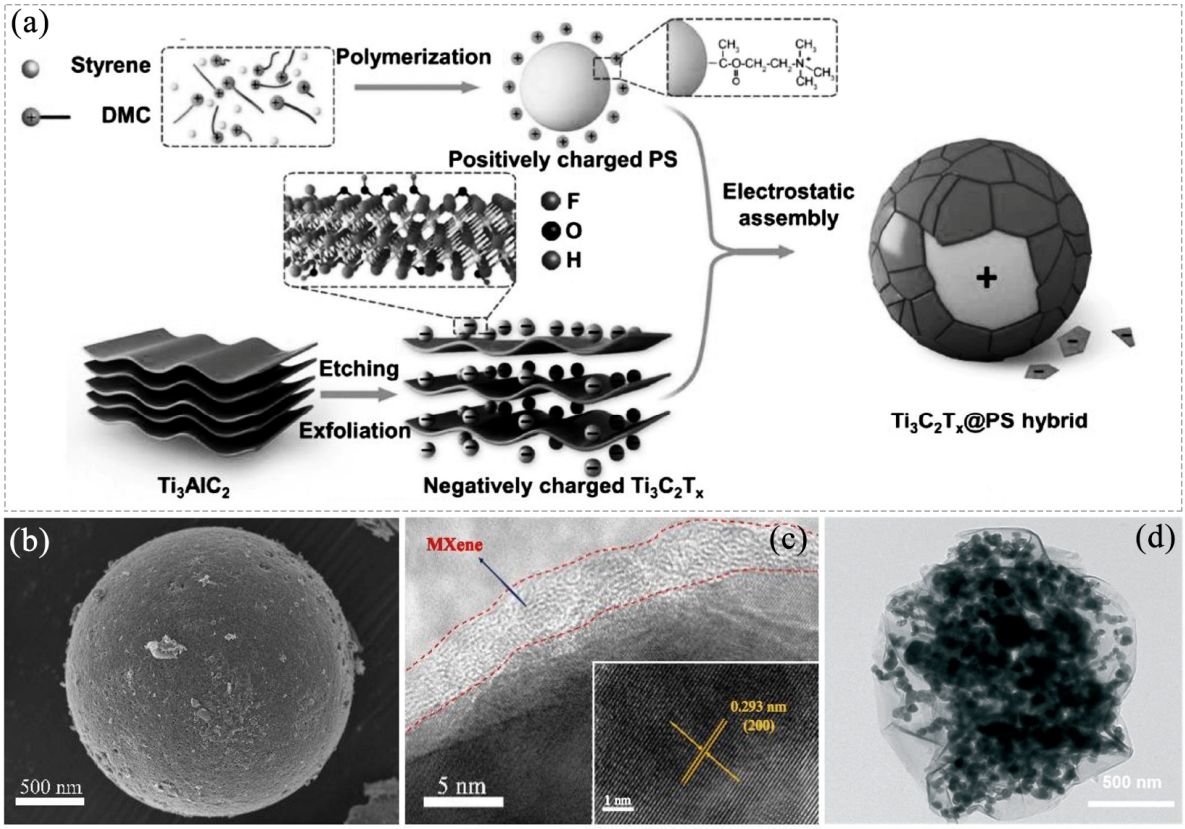


Figure 4. The preparation and morphology of the 0D MXene composite. (**a**) Schematic for the preparation of the $Ti_3C_2T_x$@PS sphere; reproduced from [48], with the permission of Wiley-VCH. (**b**,**c**) $CoSe_2$@MXene; reproduced from [4], with the permission of Royal Society of Chemistry. (**d**) SnO_2@MXene; reproduced from [50], with the permission of Royal Society of Chemistry.

3.1.2. Hydrogen-Bond-Driven Self-Assembly

Hydrogen bonds are local interactions in the form of X–H. . .A, where the X–H group is polar due to the offset shared electrons. Thus, hydrogen atoms in the protonation state will attract electronegative atoms (A) via Coulomb interactions. The surface terminations give MXenes the opportunity to assemble into multi-dimensional structures via hydrogen bonding [51]. Polymethyl methacrylate (PMMA) with hydroxyl groups can drive MXene nanosheets to assemble into PMMA@MXene microspheres via hydrogen bonding [52]. Laminated MXene nanosheets are observed on the surface of the microsphere. Furthermore, as the pyrolysis temperature of PMMA is not high, it can be removed via heat treatment in an inert atmosphere to fabricate MXene hollow spheres [53]. The removal of PMMA has no significant effect on the morphology of the microspheres, and MXene nanosheets still maintain the 0D structure. Based on this mechanism, the further deposition of magnetic metal ions via electrostatic adsorption can produce magnetic 0D MXene structures [29]. Through the alternative assembly process, magnetic 0D MXene structures can integrate dielectric and magnetic phases alternately.

3.1.3. Covalent Bonds Drive Self-Assembly

Compared with electrostatic interactions and hydrogen bonding, covalent bonding is the tightest. There are two main strategies for designing covalent bonding with respect to the assembly of MXene nanosheets: direct bonding and functionalization. For direct bonding, terminations (–O, –OH and –F) on the MXene surface play a bridging role for in situ bonding [54]. Figure 4d shows a core–shell system constructed by the direct bonding of SnO_2 and MXene [50]. The translucent MXene shell links with plenty of SnO_2 nanoparticles via S–O–Ti bonds, greatly improving the stability of this core–shell system. For function-

alization, modifying and customizing the terminations is required before bonding [55]. For example, alkali treatment can make –OH terminations predominate on the surface of MXene; thus, MXene nanosheets are able to covalently bond with phosphorus [56]. Grafting amino groups onto the surface is another way to increase the activity of MXene. Via the amidation reaction between amino-functionalized $Ti_3C_2T_x$ and graphene oxide (GO), covalently bonded MXene and reduced graphene oxide (rGO) composites are obtained [57].

3.2. One-Dimensional Structures

3.2.1. Template-Based Method

Similarly to 0D MXene structures, template-based self-assembly via atomic/molecular interactions also holds for constructing 1D MXene structures. Carbon fiber, an accessible 1D material, can act as a template for assembling 1D MXene structures. However, the solid binding of carbon fibers to MXene nanosheets is an issue because of the lack of cations on its surface, where surface modification is required. Figure 5a shows carbon fiber with a positive charge after cetyltrimethylammonium bromide modification [6]. Thus, the electrostatic attraction drives the MXene nanosheets to wrap around the carbon fiber, forming the core–sheath carbon fiber@MXene.

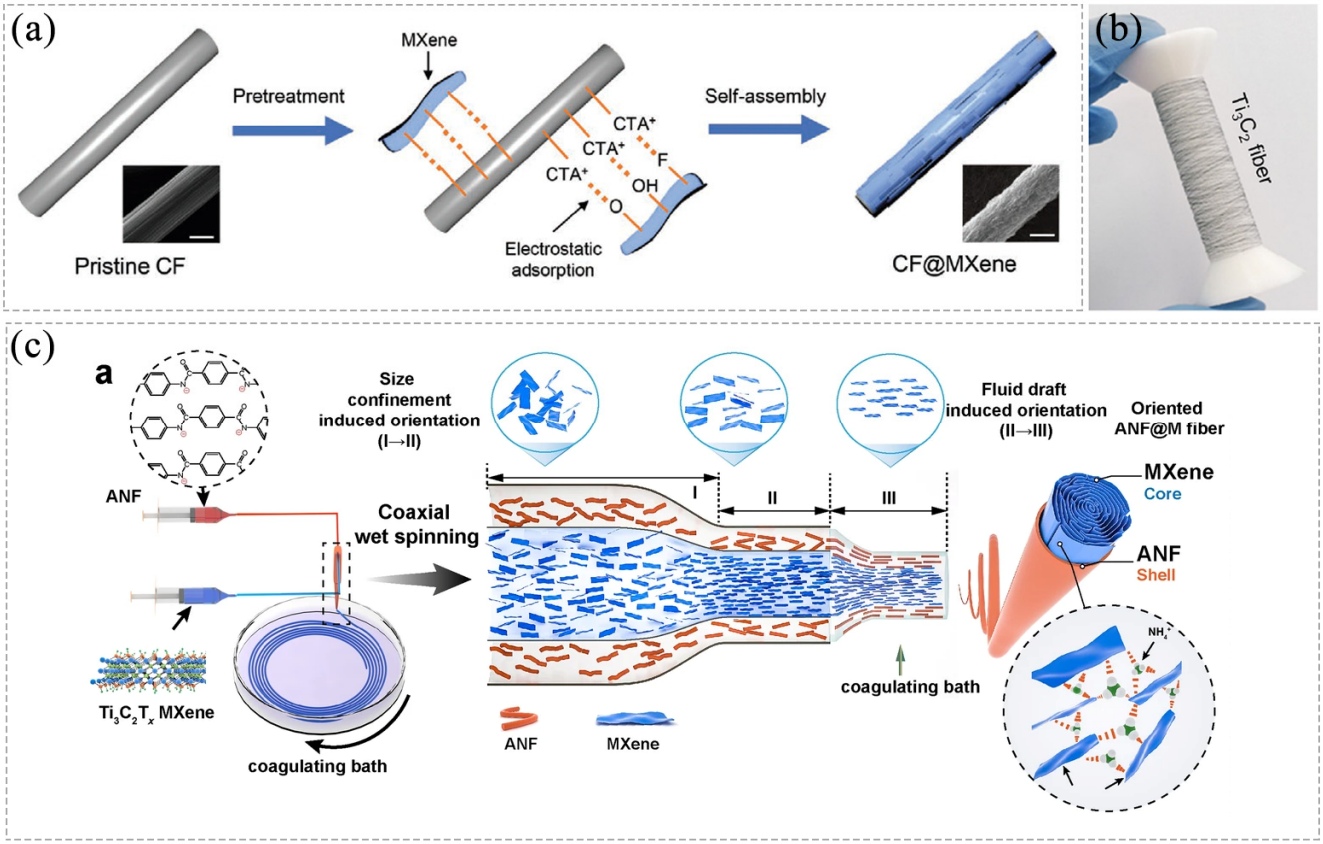


Figure 5. The preparation and morphology of the 1D MXene composite fiber. (**a**) Schematic for the preparation of carbon fiber@MXene; reproduced from [6], with the permission of Wiley-VCH. (**b**) Ti_3C_2 fiber; reproduced from [58], with the permission of the American Chemical Society. (**c**) Schematic for the preparation of core–shell aramid@MXene fibers; reproduced from [5], with the permission of the authors, published by Springer Nature.

3.2.2. Spinning

Spinning, the process of extruding material from the fine spinneret to form filaments, includes wet spinning and electrospinning. For wet spinning, the extruded fibers are solidified by dipping them into a coagulation bath, while, for electrospinning, the collector

comprises grounded metal. Generally, the diameter of the spun fiber is dominated by the diameter of the spinneret, extrusion rate, receiving distance, liquid viscosity, etc.

MXene nanosheets can spontaneously form nematic phases in a certain space due to the large aspect ratio and surface charge. This is very suitable for the application of wet spinning. The concentration transition from a disordered state to the nematic phase of the $Ti_3C_2T_x$ nanosheet is inversely proportional to the lateral size of the nanosheet [58]. In the preparation process, the size of $Ti_3C_2T_x$ nanosheets separated via the centrifugal method is large, up to 3.1 μm; thus, the nanosheets' transition concentration is low (13.2 mg/mL). The size of the nanosheets separated via sonication is small, and the corresponding transition concentration is higher, reaching 66.3 mg/mL. Therefore, pure liquid crystal $Ti_3C_2T_x$ can be converted into 1D fiber via the wet spinning method, as shown in Figure 5b. In addition to $Ti_3C_2T_x$, $Mo_2Ti_2C_3$ and Ti_2C also exist in liquid crystal states, on which wet spinning can be applied to fabricate 1D fiber. However, wet-spun liquid crystal MXene has a tensile strength of 40.5 MPa, resulting in low spinnability. Materials with high mechanical strength, such as polymers containing long molecular chains, can be introduced to improve their mechanical properties. Liu et al. introduced aramid nanofibers (ANF) into $Ti_3C_2T_x$ via coaxial wet spinning, as shown in Figure 5c, where the aramid shell and core are bonded by hydrogen bonds [5]. Subsequently, the coaxial ANF@$Ti_3C_2T_x$ fiber is coagulated via the NH_4Cl solution. Positively charged NH^{4+} ions can cross-link the nanosheets via electrostatic attraction, further enhancing the stability of the coaxial fiber. The MXene nanosheets are arranged very neatly. This is attributed to the induced shear force generated by the liquid's flow relative to the gradually narrowing spinneret. The tensile strength of this coaxial MXene fiber is 380.1 MPa, significantly higher than that of pure liquid crystal MXene. Therefore, besides introducing a second phase material, the composition of the coagulation bath and the assembly arrangement of MXene nanosheets both affect the morphology and mechanical properties of 1D MXene structures.

Different from wet spinning, electrospinning is carried out under the action of a strong electric field, where the electrostatic repulsion force shapes the fiber [59]. Under an electric field, nanoscale MXene composite fibers are achieved, of which the diameter can be tuned via the loading concentration of MXene nanosheets, rate of extrusion, needle gauge and solution viscosity. Levitt et al. combined electrospinning with wet spinning, and they explored novel one-step bath electrospinning [60]. They added a coagulation bath between the spinneret and the receiver. The spinning syringe is filled with a nylon polymer solution, while the coagulation bath is filled with the MXene dispersion. When the electrospun nylon polymer enters the MXene dispersion, the counterdiffusion of the solvent and water molecules traps MXene nanosheets among the filaments. This method greatly improves the loading capacity of MXene up to 90 wt.%.

3.3. Two-Dimensional Structures

Films can be directly applied to fabricate wearable devices like cloth. The preparation methods of MXene films of different thicknesses are widely investigated [61]. For MXene films with a thickness of a few nanometers, evaporative self-assembly and spin coating can be selected. For MXene films with a thickness of hundreds of nanometers, spraying is a simple preparation method. For MXene films with a thickness of a few microns, vacuum-assisted filtration attracts extensive attention.

3.3.1. Evaporative Self-Assembly

Rayleigh–Benard convection provides conditions for assembling 2D nanomaterials, such as graphene and MXenes. When volatile solvent evaporates, the temperature difference between the upper and lower sides of the fluid induces convection [62]. Vertical convection propels $Ti_3C_2T_x$ nanosheets towards the surface of the solution, and lateral convection drives MXene nanosheets to aggregate and overlap. As shown in Figure 6a, the self-assembled MXene nanosheets overlap very densely on the liquid surface, forming a

single layer of MXene film over a large area. This method allows the precise control of the number of MXene layers, and a nanoscale MXene film is obtained.

3.3.2. Spraying

Spraying is a strategy for preparing submicron 2D MXene films over a large area. During spraying, the MXene-based solution is sprayed from a container via external forces onto a substrate [63,64]. Fabrics with good mechanical properties are excellent candidates for this substrate [7,65]. However, many fabrics have poor hydrophilicity and are difficult to combine with MXene. It is necessary to activate the surface of fabrics via hydrophilic groups or polar groups to ensure the stable adhesion of MXenes to the fabrics. For example, the surface of aramid nonwoven fabrics is hydrophilic after plasma treatment; thus, the sprayed MXene is adsorbed on its surface via hydrogen bonding (Figure 6b) [66]. MXene-modified nonwovens possess not only the advantages of flexibility and the tensile strength of the nonwoven fabric but also the flame-retardant property of MXene, showing potential in wearable devices (Figure 6c).

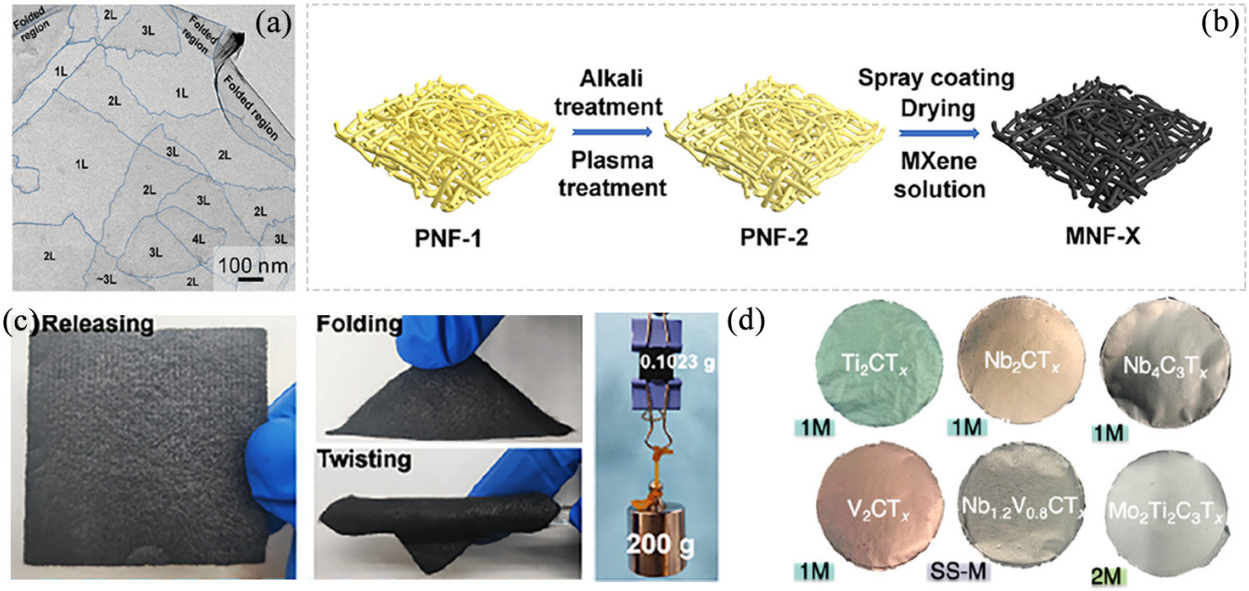


Figure 6. The morphology and preparation of the 2D MXene composite film. (**a**) TEM image of assembled MXene film; reproduced from [62], with the permission of Wiley-VCH. (**b**) Preparation process of the MXene-coated nonwoven material. (**c**) Flexible MXene-modified nonwoven materials; reproduced from [66], with the permission of Elsevier. (**d**) Filtrated MXene films; reproduced from [67], with the permission of the American Chemical Society.

3.3.3. Vacuum-Assisted Filtration

Vacuum filtration is a mechanical method that accelerates the seepage of water in MXene dispersion via the negative pressure caused by pumping, and the remaining MXene nanosheets can be stacked into films on account of the capillary compression force. Compared with evaporative self-assembly and spraying methods, the filtered film is thicker and measures up to the micrometer scale. Figure 6d illustrates the filtrated films from six different MXenes, including Ti_2CT_x, V_2CT_x, Nb_2CT_x, $Nb_{1.2}V_{0.8}CT$, $Nb_4C_3T_x$ and $Mo_2Ti_2C_3T_x$ [67]. The variation in the color of freestanding films results from the different optical properties of MXenes. The mechanical reliabilities of filtrated freestanding films are only determined by the intrinsic strength of MXene composites because micrometer-thick films do not need to be attached to a substrate. Voids among MXene platelets play a major role in influencing the mechanical strength of films. For pure MXene films, their mechanical strength depends on the interlayer sliding of platelets [68]. For MXene composite films, the interactions among MXene nanosheets and heterogeneous phases dominate the me-

chanical strength [69]. The sequential bridging of hydrogen and covalent bonds on MXene nanosheets is an available method for producing compact and aligned MXene films [70]. Compared with hydrogen-bonded MXene (HBM) or covalent-bonded MXene (CBM), the sequentially bridged MXene (SBM) film has the highest mechanical strength, with a tensile strength of 583 ± 16 MPa. Usually, the filtration time of MXene is slow at several hours. In order to improve production efficiency, various electrolytes, such as KOH, NaOH and NaCl, are introduced. The ions in these electrolytes can induce the formation of MXene microgels, and the microgels' gaps are conducive to the rapid seepage of water [71]. Then, filtration times can be compressed into tenths of seconds, and production efficiency is increased sharply. It is noted that the simultaneous introduction of electrolytes and bonds into the MXene solution is of great significance for the rapid fabrication of large-scale MXene films. In addition to the above methods, dip-coating, hot pressing and multilayered casting methods are available strategies for preparing 2D MXene films [72–74].

3.4. Three-Dimensional Structures

3.4.1. In Situ Growth

Since the surface functional groups of MXene are attractive to some metal cations via electrostatic interaction or ion exchange, materials containing metal ions, such as metal salts and MOFs, can be adsorbed by MXene nanosheets [75]. In addition to providing a metal source, metal ions also have an additional function. They act as a catalyst that promotes the subsequent reaction. For example, in the in situ growth of ZIF-67 on the $Ti_3C_2T_x$ nanosheet, Co^{2+} is attracted by the terminations of $Ti_3C_2T_x$ [76]. Via further pyrolysis, carbon nanotubes are formed to link reduced cobalt and $Ti_3C_2T_x$, where Co serves as a catalyst to catalyze the growth of carbon nanotubes, and carbon is a reducing agent that reduces Co ions. Then, 0D Co nanoparticles, 1D C nanotubes and 2D $Ti_3C_2T_x$ nanosheets are combined to construct a multi-level architecture. This type of growth, similarly to seed germination, is also suitable for Ni^{2+} [77].

3.4.2. Freeze Drying

The freeze-drying technique uses ice as a template to shape MXenes in order to create 3D architectures [78]. In the vacuum environment, the ice sublimates directly from the solid without melting processes, and the dried material can retain its porous structure. In order to obtain a product with a uniform skeleton, preventing MXene from accumulating during freeze drying is crucial. As shown in Figure 7a, cellulose nanofiber (CNF) can assist the freeze-drying process to fabricate ultra-lightweight MXene skeleton structures, since the hydrogen bond between cellulose and MXene can effectively prevent the accretion of $Ti_3C_2T_x$ nanosheets [79]. As the ice grows from the bottom upwards, the arrangement of the cells formed by $Ti_3C_2T_x$ nanosheets is orientated (Figure 7b). The average size of the cells can be modulated by the volume fraction of $Ti_3C_2T_x$ (Figure 7c) because an increase in MXene can create more nucleation sites to limit ice growth. Electrostatic repulsion can also prevent MXene from accumulating during the freeze-drying process. Figure 7d shows that the MXene–graphene oxide solution displays a stronger Tyndall effect compared with that of the MXene solution [80]. This is attributed to the strong electrostatic repulsion between negatively charged MXene and graphene oxide nanosheets. Thus, the freeze-dried MXene–graphene oxide foam with a uniform skeleton structure exhibits better electrical conductivity and electromagnetic performance.

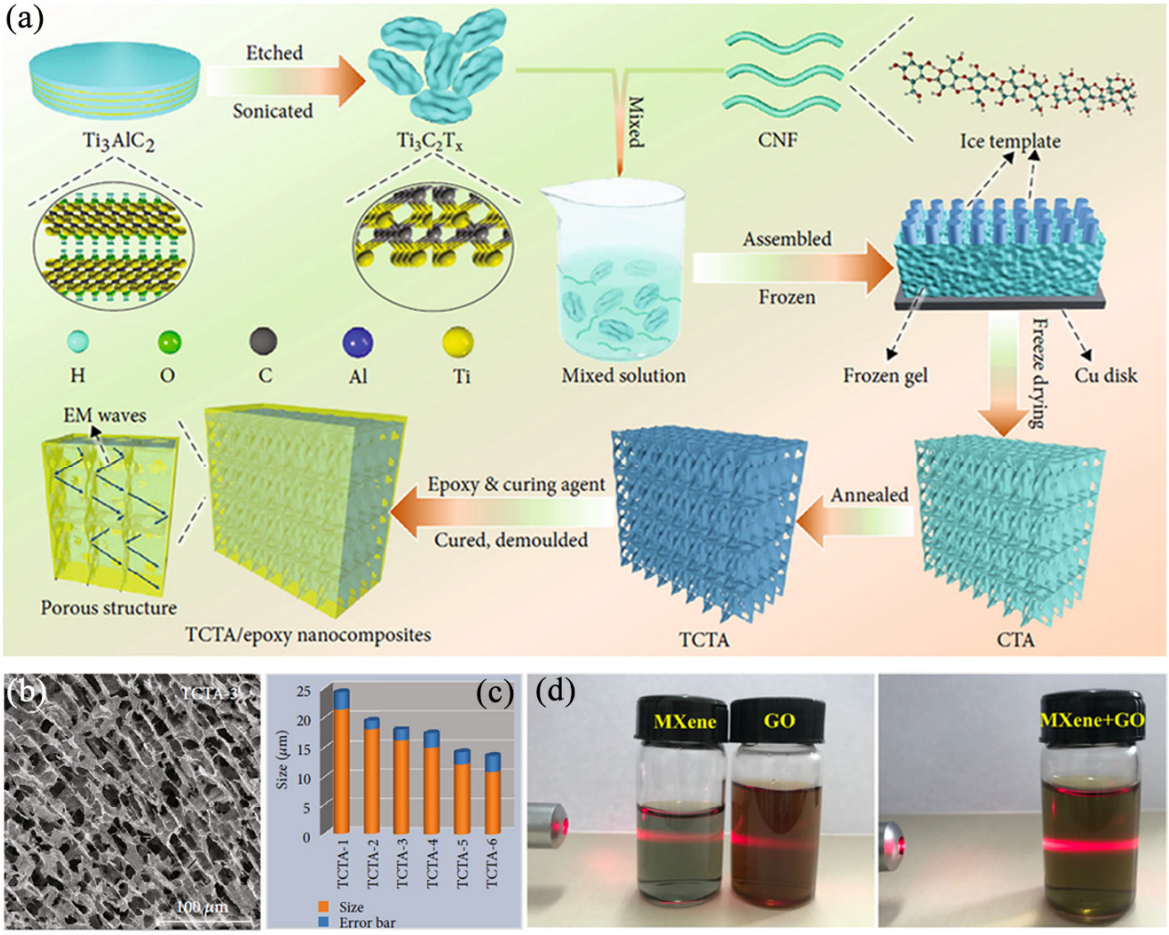


Figure 7. The preparation and microstructure of the 3D MXene composite. (**a**) Schematic for the freeze-drying process followed by annealing. (**b**) SEM image of the annealed cellulose/$Ti_3C_2T_x$ aerogel. (**c**) Average cell sizes with increasing MXene contents; reproduced from [79], with the permission of the authors, published by American Association for the Advancement of Science. (**d**) Comparison of the Tyndall effect of MXene, GO and MXene/rGO solutions; reproduced from [80], with the permission of Elsevier.

4. Electromagnetic Attenuation Performance

4.1. Electromagnetic Absorption Performance of Multi-Dimensional MXenes

Ultra-wideband, multi-band, lightweight and thin electromagnetic absorbing materials comprise the research frontiers in this field [81]. The absorption frequencies of current MXene composites can be achieved in the S band, C band, X band and Ku band [82–84]. Assembling MXene into aerogel microspheres is a sound strategy to reduce the materials' weight and improve electromagnetic absorption by tuning impedance matching due to the abundant ventages [85]. Hollow spheres are other candidates for lightweight microwave absorption materials. As mentioned above, the PMMA sphere can be used as a sacrificial template to prepare hollow MXene microspheres. Based on this, Wang et al. assembled ZnO nanoarrays on the hollow MXene microsphere, as shown in Figure 8a [86]. When the pyrolysis temperature is increased, the average ε'' values of the composites increase from 1.16 to 3.23 due to the increased polarization of ZnO (Figure 8b). The tan δ_e shows that the electromagnetically dissipated capability of $Ti_3C_2T_x$@ZnO-650 is the strongest by integrating the strong polarization loss advantages of the ZnO nanoarrays and high conduction loss advantages of MXene nanosheets (Figure 8c). Thus, the $Ti_3C_2T_x$@ZnO-650 microspheres obtain an excellent microwave absorption of −57.4 dB at 2 mm in the Ku band and an effective absorption bandwidth of 6.56 GHz (Figure 8d). Introducing a magnetic phase not only enhances the magnetic responses but also inspires multi-scale interfaces.

For example, adding Fe_3O_4 nanoparticles into flower-like rGO/MXene microspheres can increase the effective absorption bandwidth [87]. Simultaneously, by controlling the amount of Fe_3O_4, the effective absorption band is shifted from the X band to the Ku band.

One-dimensional materials with a high aspect ratio have natural long-range conductive channels that increase conductivity loss [88]. Figure 8e shows the C@MXene fiber prepared via the template method [6]. CF is the abbreviation for carbon fiber. CM-1, CM-2, CM-3 and CM-4 are abbreviations for C@MXene with $Ti_3C_2T_x$ at 5, 10, 15 and 20 wt.p%, respectively. It is noted that both ε' and ε'' increase with the addition of $Ti_3C_2T_x$ (Figure 8f,g). Multiple peaks in ε'' indicate the relaxation behaviors of the terminations of $Ti_3C_2T_x$ and the residual groups in carbon fiber. The corresponding electromagnetic absorption performance is shown in Figure 8h. When the sample's thickness exceeds 2 mm, CM-3 exhibits the minimum reflection loss. This is attributed to the matched impedance of CM-3, resulting from the homogeneous coverage of $Ti_3C_2T_x$ nanosheets.

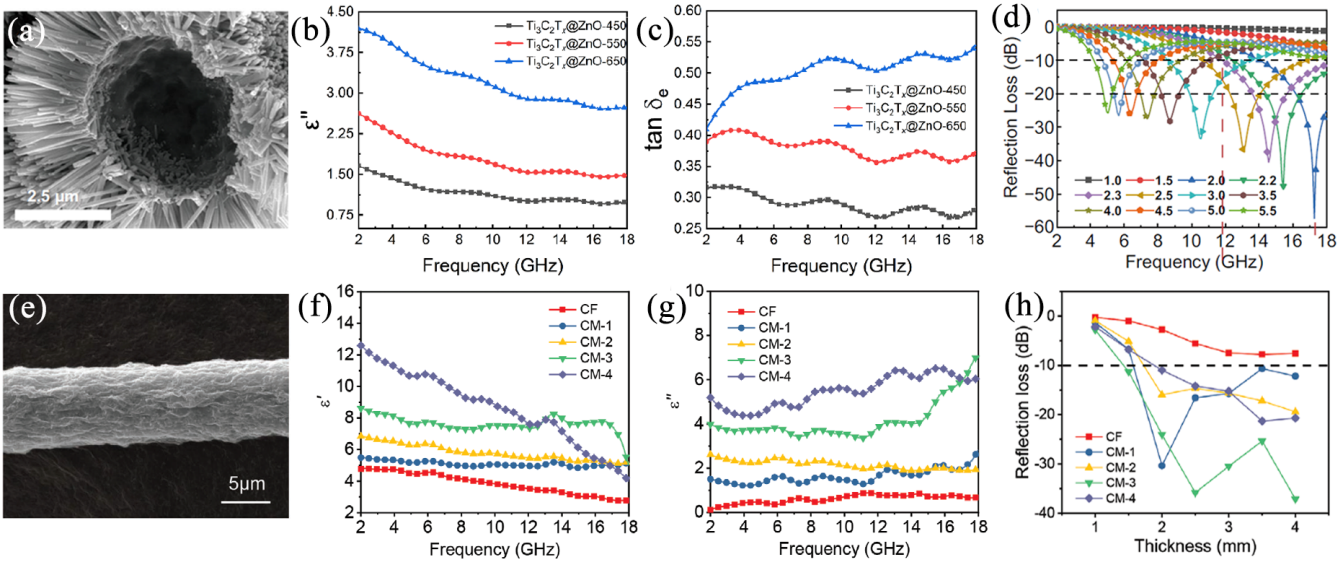


Figure 8. The morphologies and electromagnetic responses of $Ti_3C_2T_x$@ZnO and C@MXene. (**a**) $Ti_3C_2T_x$@ZnO hollow sphere. (**b**) Imaginary permittivity. (**c**) tan δ_e. (**d**) Electromagnetic absorption performance; reproduced from [86], with the permission of the authors, published by Springer Nature. (**e**) 1D C@MXene. (**f**) Real permittivity. (**g**) Imaginary permittivity. (**h**) Electromagnetic absorption performance; reproduced from [6], with the permission of Wiley-VCH.

MXene, as a 2D nanosheet, has mitigative restacking issues during the filtration process, which is not conducive to the density and electromagnetic properties of the film. Li et al. designed a combined method of electrostatic self-assembly and vacuum filtration to suppress this issue [89]. After diallyldimethylammonium chloride (PDDA) treatment, CoNi-decorated rGO nanosheets are positively charged with a zeta potential of +50.12 mV, which can act as an intercalation to electrostatically attract MXene's self-assembly. Pure MXene films have an excessive dielectric loss due to the inherent high conductivity, and their surface reflection is strong. Compared with the pure MXene film, ε' and ε'' of MXene-rGO/CoNi film decrease because the micro-continuous MXene structure is destroyed by intercalated rGO. Therefore, the MXene-rGO/CoNi film with magnetic loss and appropriate dielectric loss displays an efficient microwave absorption of −54.1 dB.

Freezing temperatures can directly affect the morphology and electromagnetic properties of 3D MXenes. As shown in Figure 9a, the densities of $Ti_3C_2T_x$ foams prepared at different prefreezing temperatures of −20, −50 and −196 °C are 7.01, 6.98 and 6.52 mg/mm^3, respectively [90]. The decreased density resultsfrom the formation of smaller ice crystals and pores under substantial undercooling. These uniform small pores display many contact sites, leading to larger contact resistance. As a result, the conductivity of the sample

prefrozen at −196 °C is the lowest, as shown in Figure 9b. The low conductivity results in reduced dielectric properties (Figure 9c), which improve the impedance matching level of the foam. Its RL is −50.6 dB at 1.8 mm. Therefore, appropriate conductivity is crucial for promoting electromagnetic absorption, and excessive conductivity will cause strong reflected waves. Figure 9d shows an MXene-based electromagnetic absorbing foam composed of $Ti_3C_2T_x/MoS_2$ self-rolling rods [10]. Different from the foams comprising pure $Ti_3C_2T_x$ and non-rolling $Ti_3C_2T_x/MoS_2$ sheets, the self-rolling structure can reduce the risk of impedance mismatching caused by high conductivity. Meanwhile, there are a large number of heterogeneous interfaces between $Ti_3C_2T_x$ and MoS_2, and polarization loss ε_p'' is significantly higher than conductivity loss ε_c'' (Figure 9e). Thus, the self-rolling $Ti_3C_2T_x/MoS_2$ composite displays a matched impedance with an RL of −52.1 dB and an effective absorption bandwidth covering the X band.

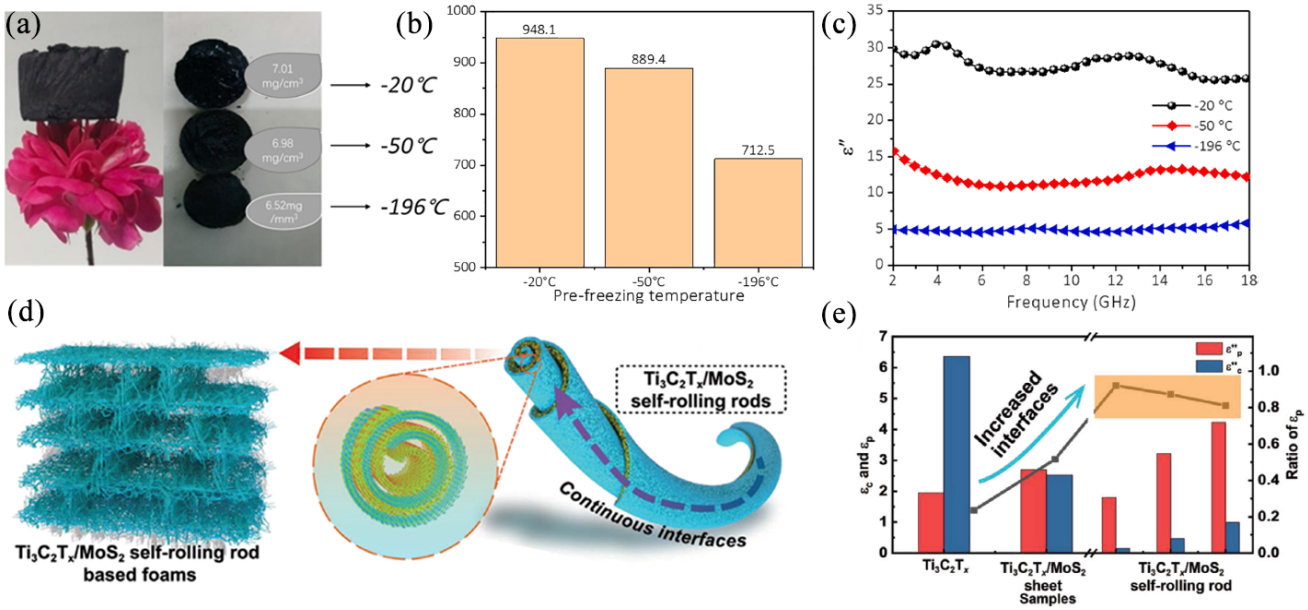


Figure 9. The morphology, electrical property and dielectric loss of $Ti_3C_2T_x$ foams. (**a**) $Ti_3C_2T_x$ foams prepared at different prefreezing temperatures. (**b**) Conductivity. (**c**) Imaginary permittivity; reproduced from [90], with the permission of Elsevier. (**d**) Schematic for the preparation process of self-rolling rod-based $Ti_3C_2T_x/MoS_2$ foam. (**e**) Comparation of conduction and polarization loss; reproduced from [10], with the permission of the authors, published by Wiley-VCH.

4.2. Electromagnetic Shielding Performance of Multi-Dimensional MXenes

For the monodispersed 0D MXene structure, electrons are localized within a limited region where long-range transmission abilities are lost; thus, the electromagnetic shielding performance of 0D MXene structure is weak due to the poor conduction loss and reflection. Generally, 0D MXene structures can realize electromagnetic shielding capability by being arranged into higher-dimensional macroscopical structures [91].

Fibers that are lightweight and tough can be employed to weave wearable devices. Figure 10a shows a wet-spun ANF@MXene coaxial fiber with a tight knot [5]. It features the following properties: super toughness (48.1 MJ/m^3) and mechanical strength (502.9 MPa). The optimized conductivity of coaxial fiber is 3.2×10^5 S/m, higher than that of neat MXene fibers (Figure 10b). When the fibers are woven in textiles, the perfect conductive network and the strong reflection result in effective electromagnetic shielding performance. As shown in Figure 10c, electromagnetic shielding performance is significantly dependent on weave density and thickness. The SE value of the textile with a mesh spacing of 1 mm and a thickness of 213 μm is up to 83.4 dB.

The content of MXene is a key factor affecting the shielding performance of a composite film, where SE is proportional to the MXene content due to the ultra-high conductivity of

MXene [92]. Similar conclusions are also demonstrated in the freeze-dried 3D MXene-rGO foam, as depicted in Figure 10d [80]. When the amounts of MXene are 25 wt.%, 33 wt.% and 50 wt.%, the corresponding conductivities are 303, 1000 and 1250 S/m, respectively, significantly higher than that of rGO foam, as shown in Figure 10e. As the density of MXene is greater than that of rGO, the composite's density is enhanced from 3.7 to 7.2 mg/cm^3 with increasing amounts of MXene. Therefore, 33 wt.% MXene composite foam presents the best SSE (SE per unit density), reaching 6217 dB cm^3/g at 1.5 mm (Figure 10f). The analysis of the power coefficient confirms that the shielding ability mainly comes from reflection.

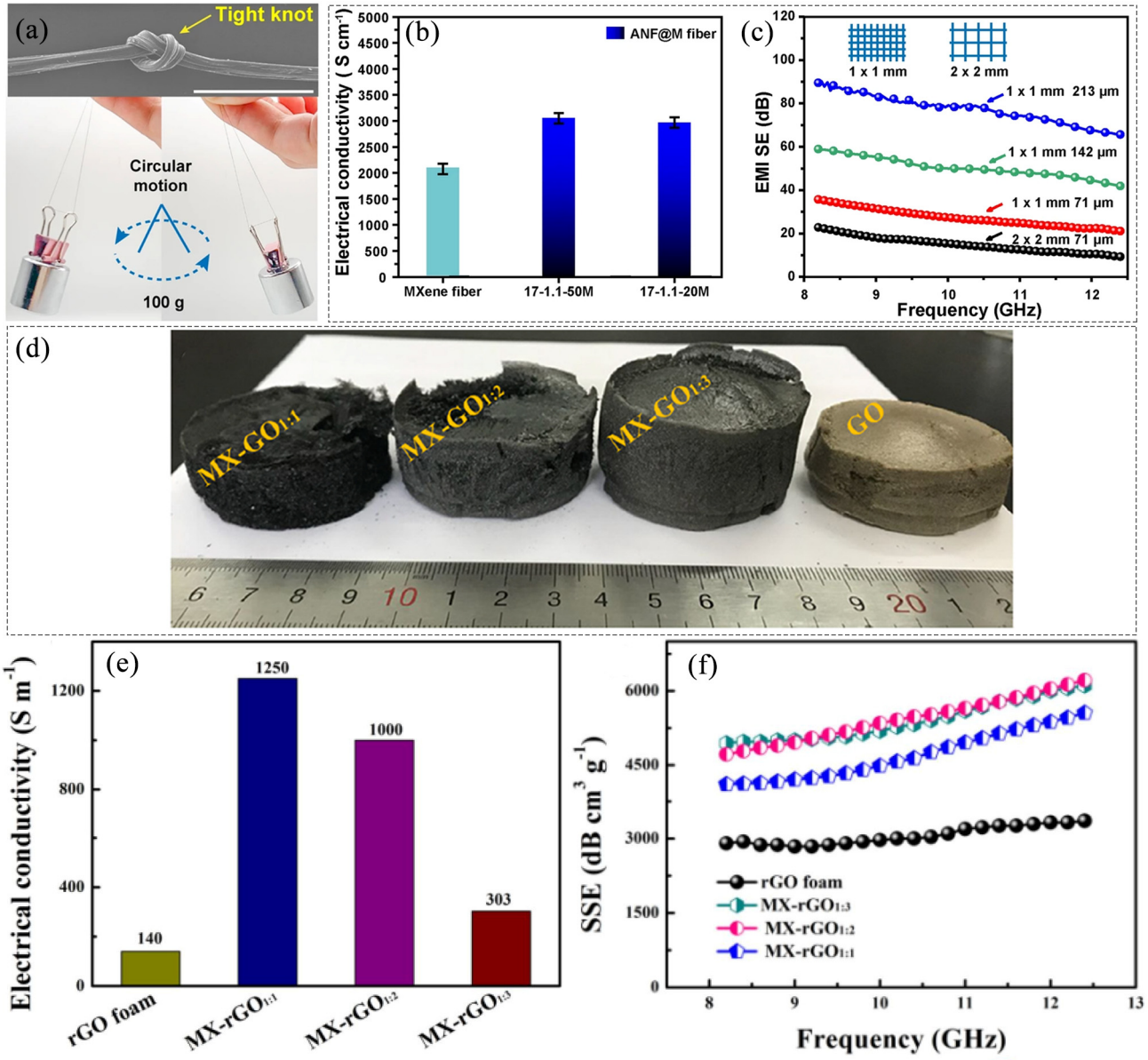


Figure 10. The morphologies, conductivities and electromagnetic interference shielding performance of 1D MXene and 3D composites. (**a**) Aramid nanofiber@MXene coaxial fibers. (**b**) Conductivities of pure MXene fiber and MXene composite fibers. (**c**) SE versus mesh grid; reproduced from [5], with the permission of the authors, published by Springer Nature. (**d**) GO and MXene/graphene (MX-GO) foams with different hybrid ratios. (**e**) Conductivities of rGO and MX-GO foams. (**f**) Shielding performance of different foams; reproduced from [80], with the permission of Elsevier.

5. Additional Extended Functionality towards Wearable Devices

Function integration has great significance for the upgrade of intelligent wearable devices. The continuous exploration of MXene's additional functions will drive wearable devices towards comfort, convenience and aesthetics. In this section, several extended functions, including thermal conversion, thermal management, self-cleaning and transparency, are shown [93–95].

5.1. Thermal Conversion

MXene films with prominent photothermal and electrothermal conversion performance exhibit application potential in wearable self-warming films [96–98]. Exfoliated Ti_3C_2 MXene has a semimetal-like energy-band structure that is similar to a metal nanoparticle; thus, it displays strong absorption with respect to near-infrared irradiation (~800 nm) due to plasmon resonance [99,100]. The high electrical property is conducive not only to the high conduction loss but also to the high extinction coefficient as well as high joule heat, which encourages the integration of photothermal and electrothermal conversions into wearable electromagnetic attenuation devices. This multifunctional electromagnetic attenuating device has potential applications in extremely cold conditions. Figure 11a compares the temperature change in pristine nonwoven fabric (PNF) and the MXene-modified PNF (MNF) placed on the arm under 100 mW/cm^2 illumination [66]. After 200 s, the temperature of the MNF increases significantly up to 60.2 °C, resulting in photo-to-heat performance. If there is a lack of light, the applied voltage can also realize self-warming functions according to Joule's law ($Q = U^2t/r$) [101]. MXene with a low resistance (r) will generate high joule heating (Q) [102]. Zhou et al. fabricated an MXene/Ag-PVA transparent film via the spray method [63]. This composite film has low sheet resistance (18.3 Ω/sq) and produces heat (in joules) that is proportional to the applied voltage, as shown in Figure 11b. The corresponding infrared images show that, when the applied voltage increases from 0V to 5V, the temperature increases from 20 °C to 80 °C.

5.2. Thermal Management

Thermal insulation can realize infrared stealth in infrared imaging detection, as infrared thermal imaging can reflect the temperature field of the surface of an object. The emergence of thermal management capabilities extends the application of MXene-based electromagnetic attenuation coverings in special environments, which can hide military targets in microwave and infrared bands or prevent ambient temperatures from increasing while protecting communication security [103]. Three-dimensional MXene foams with high porosity contain air; thus, thermal conductivity is extremely decreased during the gas phase [104]. At present, Ni-MXene/melamine foam with both electromagnetic absorption and infrared stealth is experimentally realized [105]. In the Ni-MXene/melamine foam, positive Ni flowers and negative MXene nanosheets are assembled via electrostatic force, and then Ni-MXene and melamine foam are combined via capillary force. The composite foam with high porosity exhibits excellent heat insulation. Figure 11c illustrates the thermal infrared image of a hand with a color of bright yellow. When Ni-MXene/melamine foam is placed on the hand, its color is almost consistent with the hand's surroundings, which is invisible during infrared detection. Pyrolysis is usually performed to treat MXene in order to prepare Ti-containing composites. If pyrolysis does not cause the collapse of the 3D porous skeleton, the pyrolyzed MXene-based composite can still maintain good thermal insulation properties.

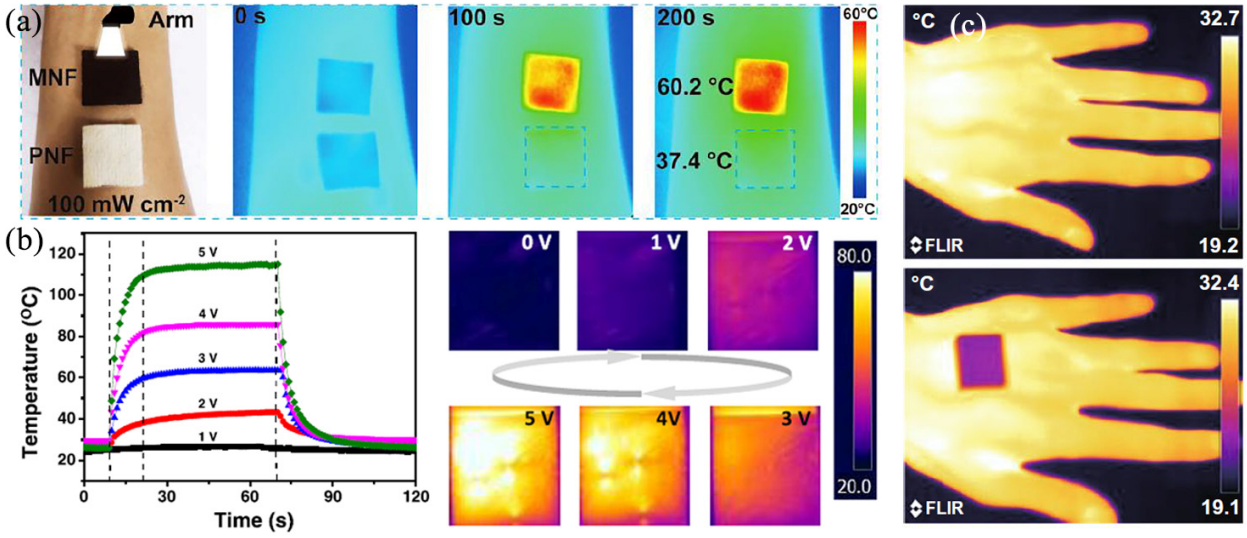


Figure 11. Thermal conversion and management capabilities of MXene composites. (**a**) PNF and MNF, as well as infrared images; reproduced from [66], with the permission of Elsevier. (**b**) Temperatures of the MXene/silver nanowire-poly(vinyl alcohol) film at 0–5 V; reproduced from [63], with the permission of the American Chemical Society. (**c**) Thermal infrared images of the Ni flower/MXene-melamine foam on the hand; reproduced from [105], with the permission of the authors, published by Springer Nature.

5.3. Self-Cleaning and Transparency

If MXene electromagnetic attenuation materials are available as radiation-proof clothing, its service life directly determines its practicality and economic value. Extended service hours relative to radiation-proof clothing are expected. Self-cleaning capabilities can lengthen the service life of wearable devices and improve the device's tolerance to the environment. Figure 12a shows a self-cleaning electromagnetic absorbing material comprising cotton fabric and $Ti_3C_2T_x$/Ni chain/ZnO array nanostructures [106]. After hydrophobic treatment with fluorinated decyl polyhedral oligomeric silsesquioxane, the nanostructures with trapped air pockets repel liquid droplets, resulting in a Cassie–Baxter state (Figure 12b). Wettability experiments demonstrate that the contact angles of common droplets such as milk, tea and water are higher than 150°. Based on this mechanism, if there are contaminants on the surface, they can also be easily carried away by water.

The optically transparent ultrathin MXene film is indispensable when constructing visual devices such as electronic screens, glasses and helmets. Figure 12c shows the optical transmittance (550 nm) of the evaporative self-assembled MXene films [62]. When the stacked layer increases from 1 to 9, optical transmittance drops from 90% to 45%. Transparent MXene composites can also be obtained by carrying out filtration on a transparent substrate. Ma et al. filtered MXene films on a transparent bacterial cellulose (BC) substrate, as shown in Figure 12d [19]. Its optical transmittance is inversely proportional to filtration times due to the stacking of MXene nanosheets. These nanometer-thin MXene films have potential in miniaturized electronics.

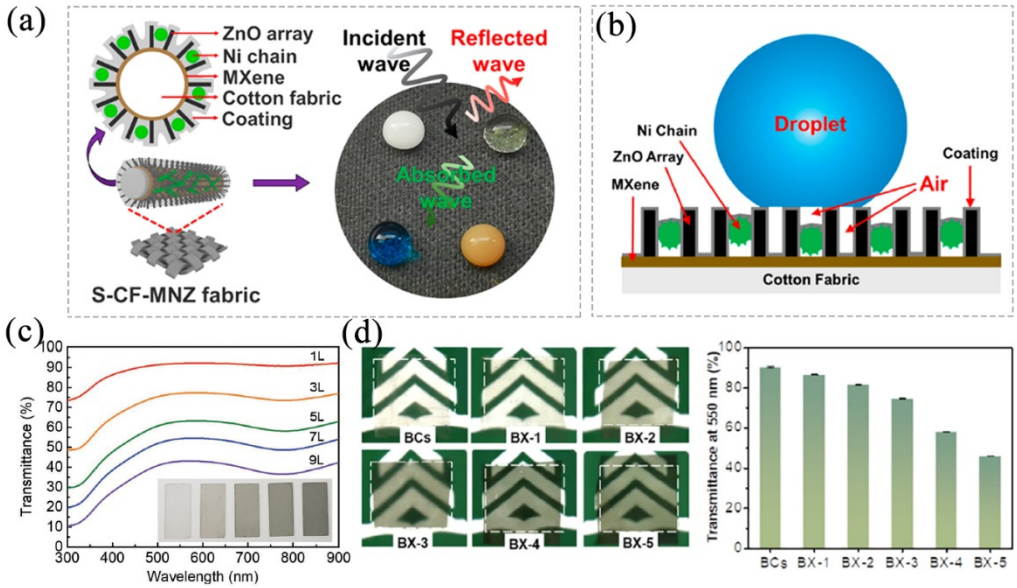


Figure 12. Self-cleaning and transparency of MXene composites. (**a**) $Ti_3C_2T_x$/Ni/ZnO nanostructures on cotton fabric for self-cleaning. (**b**) Schematic for liquid droplets on the composite fabric; reproduced from [106], with the permission of the American Chemical Society. (**c**) Transmittance of MXene films with layer numbers 1–9; reproduced from [62], with the permission of Wiley-VCH . (**d**) Transmittance of celluloses/MXene films; reproduced from [19], with the permission of Elsevier.

6. Summary and Outlook

This review analyzed the electromagnetic absorbing and interference mechanism of MXene composites, summarized the construction method of multi-dimensional MXenes and discussed the application of multi-dimensional MXenes in wearable electromagnetic attenuating devices. Multi-dimensional MXenes are successfully assembled using interfacial assemblies, spinning, vacuum-assisted filtration, freeze drying, etc., exhibiting prominent electromagnetic absorption and interference shielding performance, as well as additional functions, as shown in Tables 1 and 2. Although significant improvements in electromagnetic performance are realized by MXene composites, some issues need to be solved in practical application.

For electromagnetic absorption performance, obtaining ultra-wideband and multiband MXene composites is difficult. We must tailor microstructures precisely in order to integrate the MXene composites of different dimensions to extend the electromagnetic response band of polarization relaxation.

For electromagnetic interference shielding performance, strong reflections will produce secondary electromagnetic radiation pollution. Broadening intrinsic absorptions to include conduction loss and polarization loss should be carried out to reduce the dangers of radiation.

For wearability, good mechanical properties are prerequisites for ensuring the normal operation of wearable devices. Flexible materials such as polymers and fabrics are competitive templates relative to wearable MXene composites but their electromagnetic responses are often weak. We should strengthen the inherent electromagnetic response of MXene composites so that the loading ratios of flexible materials added can be increased.

In the future, we should not limit our focus to a single electromagnetic absorption or electromagnetic shielding function of MXene composites. We should broaden our horizons and find suitable MXene composite structures in order to achieve integrated functions, which can accelerate electromagnetic MXene attenuation devices to address diverse practical applications and complex environments.

Table 1. Comparison of electromagnetic absorption performances relative to MXene composites.

Dimensionality	Materials	Thickness (mm)	RL_{min} (dB)	Optimum Absorption Frequency	Refs.
0	$Ti_3C_2T_x$@GO	1.2	−49.1	Ku	[85]
0	SiO_2@ $Ti_3C_2T_x$	1.3	−58.01	Ku	[83]
0	$Ti_3C_2T_x$@ZnO	2	−57.4	Ku	[86]
0	$Ti_3C_2T_x$@Ni	1.5	−59.6	Ku	[29]
0	RGO/$Ti_3C_2T_x$/Fe_3O_4	2.9	−51.2	X	[87]
1	C@$Ti_3C_2T_x$@MoS_2	3.5	−61.51	C	[6]
1	$Ti_3C_2T_x$/CoNi/C	1.6	−51.6	Ku	[88]
2	$Ti_3C_2T_x$/Ni/ZnO	2.8	−35.1	X	[106]
3	NiCo Compound@ $Ti_3C_2T_x$	1.7	−67.22	Ku	[82]
3	MoS_2/$Ti_3C_2T_x$	4.53	−61.65	S	[25]
3	$Ti_3C_2T_x$@MoS_2	2.2	−60.2	Ku	[20]
3	$Ti_3C_2T_x$@Fe_2O_3	1.97	−18.6	Ku	[20]
3	CoO/MCo_2O_4/$Ti_3C_2T_x$ (M = Fe, Cu, Zn)	1.9	−52.67	Ku	[81]
3	$NiSe_2$-$CoSe_2$@C/$Ti_3C_2T_x$	2.6	−60.46	X	[14]
3	$NiCo_2O_4$-$Ti_3C_2T_x$	1.7	−72.3	Ku	[26]

Table 2. Comparison of electromagnetic shielding performances relative to MXene composites.

Dimensionality	Materials	Thickness (mm)	SE_{max} (dB)	Additional Functions	Refs.
1	Aramid@$Ti_3C_2T_x$	0.213	83.4	-	[5]
2	$Ti_3C_2T_x$	0.00004	21	-	[67]
2	$Ti_3C_2T_x$	0.000055	20	-	[62]
2	$Ti_3C_2T_x$/Ag silk	0.12	54	Humidity response	[7]
2	$Ti_3C_2T_x$/amarid	0.0141	48	Electrothermal conversion	[96]
2	Chitosan/$Ti_3C_2T_x$	0.035	40.8	Thermal management Electrothermal conversion	[44]
2	Poly(vinyl alcohol)/$Ti_3C_2T_x$	0.027	44.4	Anti-dripping	[73]
2	$Ti_3C_2T_x$/thermoplastic polyurethane	0.052	50.7	Thermal management Electrothermal conversion	[18]
2	Phosphorylated $Ti_3C_2T_x$/polypropylene/polyethylenimine	0.4	90	Flame retardancy	[72]
2	Polymerized polypyrrole/$Ti_3C_2T_x$-poly(ethylene terephthalate) coated by silicone	1.3	90	Electrothermal conversion	[74]
2	$Ti_3C_2T_x$/Aramid	1.04	35.7	Electrothermal conversion Photothermal conversion	[66]
2	$Ti_3C_2T_x$/Ag-poly(vinyl alcohol)	0.01	32	Electrothermal conversion Photothermal conversion	[63]
2	Cellulose@$Ti_3C_2T_x$@Ag	0.035	55.9	Photothermal conversion	[8]
3	$Ti_3C_2T_x$	1	69.2	-	[39]
3	$Ti_3C_2T_x$/cellulose nanofibrils	2	35.5	-	[12]
3	$Ti_3C_2T_x$@wood	10	72	-	[107]
3	$Ti_3C_2T_x$/multiwall carbon nanotubes	3	103.9	-	[42]
3	$Ti_3C_2T_x$/aramid	1.9	56.8	-	[108]
3	$Ti_3C_2T_x$/aramid	2.5	65.5	Flame retardant Thermal management	[109]
3	Polydimethylsiloxane-coated $Ti_3C_2T_x$/sodium alginate	2	70.5	-	[45]
3	Ni/$Ti_3C_2T_x$-melamine foam/polyethylene glycol	2	34.6	Electrothermal conversion Photothermal conversion	[104]
3	Fe_3O_4@$Ti_3C_2T_x$/graphene/poly (dimethylsiloxane)	1	80	Pressure sensing	[110]
3	Polydimethylsiloxane/$Ti_3C_2T_x$@polyaniline/Polypropylene	12	39.8	Reversible compressibility	[91]

Author Contributions: M.Z.: conceptualization, investigation and writing—original draft. M.-S.C.: supervision and writing—review and editing. All authors have read and agreed to the published version of the manuscript.

Funding: This work was supported by the National Natural Science Foundation of China (Nos. 52203348, 52373280 and 52273257), the Research Foundation for Youth Scholars of Beijing Technology and Business University (QNJJ2022-43) and the R&D Program of Beijing Municipal Education Commission (KM202310011001).

Conflicts of Interest: The authors declare no conflict of interest.

References

1. Guo, J.N.; Si, Y.F.; Song, R.G.; Zu, H.R.; Xin, Y.T.; Ye, D.; Xu, M.; Li, B.W.; He, D.P. High-Conductivity MXene Film-Based Millimeter Wave Antenna for 5G Applications. *Crystals* **2023**, *13*, 1136. [CrossRef]
2. Shahzad, F.; Alhabeb, M.; Hatter, C.B.; Anasori, B.; Hong, S.M.; Koo, C.M.; Gogotsi, Y. Electromagnetic interference shielding with 2D transition metal carbides (MXenes). *Science* **2016**, *353*, 1137–1140. [CrossRef]
3. Yang, S.H.; Lee, Y.J.; Kang, H.; Park, S.K.; Kang, Y.C. Carbon-Coated Three-Dimensional MXene/Iron Selenide Ball with Core-Shell Structure for High-Performance Potassium-Ion Batteries. *Nano-Micro Lett.* **2022**, *14*, 17. [CrossRef]
4. Hong, L.; Ju, S.L.; Yang, Y.H.; Zheng, J.N.; Xia, G.L.; Huang, Z.G.; Liu, X.Y.; Yu, X.B. Hollow-shell structured porous $CoSe_2$ microspheres encapsulated by MXene nanosheets for advanced lithium storage. *Sustain. Energy Fuels* **2020**, *4*, 2352–2362. [CrossRef]
5. Liu, L.X.; Chen, W.; Zhang, H.B.; Ye, L.X.; Wang, Z.G.; Zhang, Y.; Min, P.; Yu, Z.Z. Super-Tough and Environmentally Stable Aramid. Nanofiber@MXene Coaxial Fibers with Outstanding Electromagnetic Interference Shielding Efficiency. *Nano-Micro Lett.* **2022**, *14*, 111. [CrossRef]
6. Wang, J.Q.; Liu, L.; Jiao, S.L.; Ma, K.J.; Lv, J.; Yang, J.J. Hierarchical Carbon Fiber@MXene@MoS_2 Core-sheath Synergistic Microstructure for Tunable and Efficient Microwave Absorption. *Adv. Funct. Mater.* **2020**, *30*, 2002595. [CrossRef]
7. Liu, L.X.; Chen, W.; Zhang, H.B.; Wang, Q.W.; Guan, F.L.; Yu, Z.Z. Flexible and Multifunctional Silk Textiles with Biomimetic Leaf-Like MXene/Silver Nanowire Nanostructures for Electromagnetic Interference Shielding, Humidity Monitoring, and Self-Derived Hydrophobicity. *Adv. Funct. Mater.* **2019**, *29*, 1905197. [CrossRef]
8. Zhou, B.; Li, Q.T.; Xu, P.H.; Feng, Y.Z.; Ma, J.M.; Liu, C.T.; Shen, C.Y. An asymmetric sandwich structural cellulose-based film with self-supported MXene and AgNW layers for flexible electromagnetic interference shielding and thermal management. *Nanoscale* **2021**, *13*, 2378–2388. [CrossRef]
9. Weng, C.X.; Wang, G.R.; Dai, Z.H.; Pei, Y.M.; Liu, L.Q.; Zhang, Z. Buckled AgNW/MXene hybrid hierarchical sponges for high-performance electromagnetic interference shielding. *Nanoscale* **2019**, *11*, 22804–22812. [CrossRef]
10. Li, M.H.; Zhu, W.J.; Li, X.; Xu, H.L.; Fan, X.M.; Wu, H.J.; Ye, F.; Xue, J.M.; Li, X.Q.; Cheng, L.F.; et al. $Ti_3C_2T_x/MoS_2$ Self-Rolling Rod-Based Foam Boosts Interfacial Polarization for Electromagnetic Wave Absorption. *Adv. Sci.* **2022**, *9*, 2201118. [CrossRef]
11. Liu, Z.W.; Liu, Z.B.; Li, G.L.; Zhao, Y.; Wang, K.; Chen, X.B. Micro-Structure and Dielectric Properties of $Ti_3C_2T_x$ MXene after Annealing Treatment under Inert Gases. *Crystals* **2023**, *13*, 1234. [CrossRef]
12. Zeng, Z.H.; Wang, C.X.; Siqueira, G.; Han, D.X.; Huch, A.; Abdolhosseinzadeh, S.; Heier, J.; Nuesch, F.; Zhang, C.F.; Nystrom, G. Nanocellulose-MXene Biomimetic Aerogels with Orientation-Tunable Electromagnetic Interference Shielding Performance. *Adv. Sci.* **2020**, *7*, 2000979. [CrossRef]
13. Zhou, B.; Song, J.Z.; Wang, B.; Feng, Y.Z.; Liu, C.T.; Shen, C.Y. Robust double-layered ANF/MXene-PEDOT:PSS Janus films with excellent multi-source driven heating and electromagnetic interference shielding properties. *Nano Res.* **2022**, *15*, 9520–9530. [CrossRef]
14. Hou, T.Q.; Jia, Z.R.; Wang, B.B.; Li, H.B.; Liu, X.H.; Chi, Q.G.; Wu, G.L. Metal-organic framework-derived $NiSe_2$-$CoSe_2$@C/$Ti_3C_2T_x$ composites as electromagnetic wave absorbers. *Chem. Eng. J.* **2021**, *422*, 130079. [CrossRef]
15. Deng, Z.M.; Tang, P.P.; Wu, X.Y.; Zhang, H.B.; Yu, Z.Z. Superelastic, Ultralight, and Conductive $Ti_3C_2T_x$ MXene/Acidified Carbon Nanotube Anisotropic Aerogels for Electromagnetic Interference Shielding. *ACS Appl. Mater. Interfaces* **2021**, *13*, 20539–20547. [CrossRef]
16. Xiang, Z.; Shi, Y.Y.; Zhu, X.J.; Cai, L.; Lu, W. Flexible and Waterproof 2D/1D/0D Construction of MXene-Based Nanocomposites for Electromagnetic Wave Absorption, EMI Shielding, and Photothermal Conversion. *Nano-Micro Lett.* **2021**, *13*, 150. [CrossRef]
17. Cao, Y.; Zeng, Z.H.; Huang, D.Y.; Chen, Y.; Zhang, L.; Sheng, X.X. Multifunctional phase change composites based on biomass/MXene-derived hybrid scaffolds for excellent electromagnetic interference shielding and superior solar/electro-thermal energy storage. *Nano Res.* **2022**, *15*, 8524–8535. [CrossRef]
18. Gao, Q.S.; Pan, Y.M.; Zheng, G.Q.; Liu, C.T.; Shen, C.Y.; Liu, X.H. Flexible multilayered MXene/thermoplastic polyurethane films with excellent electromagnetic interference shielding, thermal conductivity, and management performances. *Adv. Compos. Hybrid Mater.* **2021**, *4*, 274–285. [CrossRef]
19. Ma, C.; Cao, W.T.; Zhang, W.; Ma, M.G.; Sun, W.M.; Zhang, J.; Chen, F. Wearable, ultrathin and transparent bacterial celluloses/MXene film with Janus structure and excellent mechanical property for electromagnetic interference shielding. *Chem. Eng. J.* **2021**, *403*, 126438. [CrossRef]

20. Wu, N.N.; Zhao, B.B.; Chen, X.Y.; Hou, C.X.; Huang, M.N.; Alhadhrami, A.; Mersal, G.A.M.; Ibrahim, M.M.; Tian, J. Dielectric properties and electromagnetic simulation of molybdenum disulfide and ferric oxide-modified $Ti_3C_2T_x$ MXene hetero-structure for potential microwave absorption. *Adv. Compos. Hybrid Mater.* **2022**, *5*, 1548–1556. [CrossRef]
21. He, P.; Cao, M.S.; Shu, J.C.; Cai, Y.Z.; Wang, X.X.; Zhao, Q.L.; Yuan, J. Atomic Layer Tailoring Titanium Carbide MXene to Tune Transport and Polarization for Utilization of Electromagnetic Energy beyond Solar and Chemical Energy. *ACS Appl. Mater. Interfaces* **2019**, *11*, 12535–12543. [CrossRef]
22. Liang, L.Y.; Han, G.J.; Li, Y.; Zhao, B.; Zhou, B.; Feng, Y.Z.; Ma, J.M.; Wang, Y.M.; Zhang, R.; Liu, C.T. Promising $Ti_3C_2T_x$ MXene/Ni Chain Hybrid with Excellent Electromagnetic Wave Absorption and Shielding Capacity. *ACS Appl. Mater. Interfaces* **2019**, *11*, 25399–25409. [CrossRef]
23. Zhou, X.J.; Wen, J.W.; Wang, Z.N.; Ma, X.H.; Wu, H.J. Broadband high-performance microwave absorption of the single-layer $Ti_3C_2T_x$ MXene. *J. Mater. Sci. Technol.* **2022**, *115*, 148–155. [CrossRef]
24. Ying, M.F.; Zhao, R.Z.; Hu, X.; Zhang, Z.H.; Liu, W.W.; Yu, J.Y.; Liu, X.L.; Liu, X.G.; Rong, H.W.; Wu, C.; et al. Wrinkled Titanium Carbide (MXene) with Surface Charge Polarizations through Chemical Etching for Superior Electromagnetic Interference Shielding. *Angew. Chem.-Int. Ed.* **2022**, *61*, e202201323. [CrossRef]
25. Yang, J.J.; Wang, J.Q.; Li, H.Q.; Wu, Z.; Xing, Y.Q.; Chen, Y.F.; Liu, L. MoS_2/MXene Aerogel with Conformal Heterogeneous Interfaces Tailored by Atomic Layer Deposition for Tunable Microwave Absorption. *Adv. Sci.* **2022**, *9*, 2101988. [CrossRef]
26. Zeng, X.J.; Zhao, C.; Yin, Y.C.; Nie, T.L.; Xie, N.H.; Yu, R.H.; Stucky, G.D. Construction of $NiCo_2O_4$ nanosheets-covered $Ti_3C_2T_x$ MXene heterostructure for remarkable electromagnetic microwave absorption. *Carbon* **2022**, *193*, 26–34. [CrossRef]
27. Gao, X.R.; Wang, B.B.; Wang, K.K.; Xu, S.; Liu, S.P.; Liu, X.H.; Jia, Z.R.; Wu, G.L. Design of $Ti_3C_2T_x/TiO_2$/PANI multi-layer composites for excellent electromagnetic wave absorption performance. *J. Colloid Interface Sci.* **2021**, *583*, 510–521. [CrossRef]
28. Hou, T.Q.; Jia, Z.R.; Wang, B.B.; Li, H.B.; Liu, X.H.; Bi, L.; Wu, G.L. MXene-based accordion 2D hybrid structure with $Co_9S_8/C/Ti_3C_2T_x$ as efficient electromagnetic wave absorber. *Chem. Eng. J.* **2021**, *414*, 128875. [CrossRef]
29. Wen, C.Y.; Li, X.; Zhang, R.X.; Xu, C.Y.; You, W.B.; Liu, Z.W.; Zhao, B.; Che, R.C. High-Density Anisotropy Magnetism Enhanced Microwave Absorption Performance in $Ti_3C_2T_x$ MXene@Ni Microspheres. *ACS Nano* **2022**, *16*, 1150–1159. [CrossRef]
30. Liang, L.Y.; Yang, R.S.; Han, G.J.; Feng, Y.Z.; Zhao, B.; Zhang, R.; Wang, Y.M.; Liu, C.T. Enhanced Electromagnetic Wave-Absorbing Performance of Magnetic Nanoparticles-Anchored 2D $Ti_3C_2T_x$ MXene. *ACS Appl. Mater. Interfaces* **2020**, *12*, 2644–2654. [CrossRef]
31. Cai, L.; Pan, F.; Zhu, X.J.; Dong, Y.Y.; Shi, Y.Y.; Xiang, Z.; Cheng, J.; Jiang, H.J.; Shi, Z.; Lu, W. Etching engineering and electrostatic self-assembly of N-doped MXene/hollow Co-ZIF hybrids for high-performance microwave absorbers. *Chem. Eng. J.* **2022**, *434*, 133865. [CrossRef]
32. Sun, C.H.; Jia, Z.R.; Xu, S.; Hu, D.Q.; Zhang, C.H.; Wu, G.L. Synergistic regulation of dielectric-magnetic dual-loss and triple heterointerface polarization via magnetic MXene for high-performance electromagnetic wave absorption. *J. Mater. Sci. Technol.* **2022**, *113*, 128–137. [CrossRef]
33. Gao, X.R.; Jia, Z.R.; Wang, B.B.; Wu, X.M.; Sun, T.; Liu, X.H.; Chi, Q.G.; Wu, G.L. Synthesis of NiCo-LDH/MXene hybrids with abundant heterojunction surfaces as a lightweight electromagnetic wave absorber. *Chem. Eng. J.* **2021**, *419*, 130019. [CrossRef]
34. Montgomery, C.G.; Dicke, R.H.; Purcell, E.M. *Principles of Microwave Circuits*; McGraw-Hill: New York, NY, USA, 1948.
35. Bird, T.S. Definition and Misuse of Return Loss. *IEEE Antennas Propag. Mag.* **2009**, *51*, 166–167. [CrossRef]
36. Wang, D.J.; Liu, Y.C.; Zhu, C.H.; Yang, G.; Liu, B.; Chen, H.F.; Cui, Y.Y.; Luo, H.J.; Gao, Y.F. Preparation of lanthanum zirconate films with a widely controllable La/Zr ratio by LCVD. *Ceram. Int.* **2018**, *44*, 10621–10627. [CrossRef]
37. Collin, R.E. *Field Theory of Guided Waves*; McGraw-Hill: New York, NY, USA, 1960.
38. Hong, Y.K.; Lee, C.Y.; Jeong, C.K.; Lee, D.E.; Kim, K.; Joo, J. Method and apparatus to measure electromagnetic interference shielding efficiency and its shielding characteristics in broadband frequency ranges. *Rev. Sci. Instrum.* **2003**, *74*, 1098–1102. [CrossRef]
39. Han, M.K.; Yin, X.W.; Hantanasirisakul, K.; Li, X.L.; Iqbal, A.; Hatter, C.B.; Anasori, B.; Koo, C.M.; Torita, T.; Soda, Y.; et al. Anisotropic MXene Aerogels with a Mechanically Tunable Ratio of Electromagnetic Wave Reflection to Absorption. *Adv. Opt. Mater.* **2019**, *7*, 1900267. [CrossRef]
40. Iqbal, A.; Sambyal, P.; Koo, C.M. 2D MXenes for Electromagnetic Shielding: A Review. *Adv. Funct. Mater.* **2020**, *30*, 2000883. [CrossRef]
41. Wan, Y.J.; Rajavel, K.; Li, X.M.; Wang, X.Y.; Liao, S.Y.; Lin, Z.Q.; Zhu, P.L.; Sun, R.; Wong, C.P. Electromagnetic interference shielding of $Ti_3C_2T_x$ MXene modified by ionic liquid for high chemical stability and excellent mechanical strength. *Chem. Eng. J.* **2021**, *408*, 127303. [CrossRef]
42. Sambyal, P.; Iqbal, A.; Hong, J.; Kim, H.; Kim, M.K.; Hong, S.M.; Han, M.K.; Gogotsi, Y.; Koo, C.M. Ultralight and Mechanically Robust $Ti_3C_2T_x$ Hybrid Aerogel Reinforced by Carbon Nanotubes for Electromagnetic Interference Shielding. *ACS Appl. Mater. Interfaces* **2019**, *11*, 38046–38054. [CrossRef]
43. Yu, Y.H.; Yi, P.; Xu, W.B.; Sun, X.; Deng, G.; Liu, X.F.; Shui, J.L.; Yu, R.H. Environmentally Tough and Stretchable MXene Organohydrogel with Exceptionally Enhanced Electromagnetic Interference Shielding Performances. *Nano-Micro Lett.* **2022**, *14*, 77. [CrossRef]
44. Tan, Z.N.; Zhao, H.; Sun, F.R.; Ran, L.X.; Yi, L.F.; Zhao, L.J.; Wu, J.R. Fabrication of Chitosan/MXene multilayered film based on layer-by-layer assembly: Toward enhanced electromagnetic interference shielding and thermal management capacity. *Compos. Part A Appl. Sci. Manuf.* **2022**, *155*, 106809. [CrossRef]

45. Wu, X.Y.; Han, B.Y.; Zhang, H.B.; Xie, X.; Tu, T.X.; Zhang, Y.; Dai, Y.; Yang, R.; Yu, Z.Z. Compressible, durable and conductive polydimethylsiloxane-coated MXene foams for high-performance electromagnetic interference shielding. *Chem. Eng. J.* **2020**, *381*, 122622. [CrossRef]
46. He, P.; Cao, M.S.; Cao, W.Q.; Yuan, J. Developing MXenes from Wireless Communication to Electromagnetic Attenuation. *Nano-Micro Lett.* **2021**, *13*, 115. [CrossRef]
47. Liu, Z.W.; Li, G.L.; Zhao, Y.; Chen, X.B. Surface Groups and Dielectric Properties of $Ti_3C_2T_x$ MXene Nanosheets after $NH_3 \cdot H_2O$ Solvothermal Treatment under Different Temperatures. *Crystals* **2023**, *13*, 1005. [CrossRef]
48. Sun, R.H.; Zhang, H.B.; Liu, J.; Xie, X.; Yang, R.; Li, Y.; Hong, S.; Yu, Z.Z. Highly Conductive Transition Metal Carbide/Carbonitride(MXene)@polystyrene Nanocomposites Fabricated by Electrostatic Assembly for Highly Efficient Electromagnetic Interference Shielding. *Adv. Funct. Mater.* **2017**, *27*, 1702807. [CrossRef]
49. Lamiel, C.; Hussain, I.; Ogunsakin, O.R.; Zhang, K.L. MXene in core-shell structures: Research progress and future prospects. *J. Mater. Chem. A* **2022**, *10*, 14247–14272. [CrossRef]
50. Wang, P.R.; Yan, Y.T.; Cheng, C.; Zhang, W.M.; Zhou, D.K.; Li, L.S.; Yang, X.W.; Liao, X.Z.; Ma, Z.F.; He, Y.S. Structural and chemical interplay between nano-active and encapsulation materials in a core-shell SnO_2@MXene lithium ion anode system. *CrystEngComm* **2021**, *23*, 368–377. [CrossRef]
51. Zhao, X.; Zha, X.J.; Tang, L.S.; Pu, J.H.; Ke, K.; Bao, R.Y.; Liu, Z.Y.; Yang, M.B.; Yang, W. Self-assembled core-shell polydopamine@MXene with synergistic solar absorption capability for highly efficient solar-to-vapor generation. *Nano Res.* **2020**, *13*, 255–264. [CrossRef]
52. Li, X.L.; Yin, X.W.; Song, C.Q.; Han, M.K.; Xu, H.L.; Duan, W.Y.; Cheng, L.F.; Zhang, L.T. Self-Assembly Core-Shell Graphene-Bridged Hollow MXenes Spheres 3D Foam with Ultrahigh Specific EM Absorption Performance. *Adv. Funct. Mater.* **2018**, *28*, 1803938. [CrossRef]
53. Zhao, M.Q.; Xie, X.Q.; Ren, C.E.; Makaryan, T.; Anasori, B.; Wang, G.X.; Gogotsi, Y. Hollow MXene Spheres and 3D Macroporous MXene Frameworks for Na-Ion Storage. *Adv. Mater.* **2017**, *29*, 1702410. [CrossRef]
54. Zhang, S.X.; Liu, H.; Cao, B.; Zhu, Q.Z.; Zhang, P.; Zhang, X.; Chen, R.J.; Wu, F.; Xu, B. An MXene/CNTs@P nanohybrid with stable Ti-O-P bonds for enhanced lithium ion storage. *J. Mater. Chem. A* **2019**, *7*, 21766–21773. [CrossRef]
55. Cao, Y.Y.; Wei, S.Q.; Zhou, Q.; Zhang, P.J.; Wang, C.D.; Zhu, K.F.; Xu, W.J.; Guo, X.; Yang, X.Y.; Wang, Y.X.; et al. Ti-Cl bonds decorated Ti_2NT_x MXene towards high-performance lithium-ion batteries. *2D Mater.* **2023**, *10*, 014001. [CrossRef]
56. Pan, Z.H.; Kang, L.X.; Li, T.; Waqar, M.; Yang, J.; Gu, Q.L.; Liu, X.M.; Kou, Z.K.; Wang, Z.; Zheng, L.R.; et al. Black Phosphorus@$Ti_3C_2T_x$ MXene Composites with Engineered Chemical Bonds for Commercial-Level Capacitive Energy Storage. *ACS Nano* **2021**, *15*, 12975–12987. [CrossRef]
57. Yang, F.X.; Huang, Y.; Han, X.P.; Zhang, S.; Yu, M.; Zhang, J.P.; Sun, X. Covalent Bonding of MXene/Reduced Graphene Oxide Composites for Efficient Electromagnetic Wave Absorption. *ACS Appl. Nano Mater.* **2023**, *6*, 3367–3377. [CrossRef]
58. Zhang, J.Z.; Uzun, S.; Seyedin, S.; Lynch, P.A.; Akuzum, B.; Wang, Z.Y.; Qin, S.; Alhabeb, M.; Shuck, C.E.; Lei, W.W.; et al. Additive-Free MXene Liquid Crystals and Fibers. *ACS Cent. Sci.* **2020**, *6*, 254–265. [CrossRef]
59. Levitt, A.S.; Alhabeb, M.; Hatter, C.B.; Sarycheva, A.; Dion, G.; Gogotsi, Y. Electrospun MXene/carbon nanofibers as supercapacitor electrodes. *J. Mater. Chem. A* **2019**, *7*, 269–277. [CrossRef]
60. Levitt, A.; Seyedin, S.; Zhang, J.Z.; Wang, X.H.; Razal, J.M.; Dion, G.; Gogotsi, Y. Bath Electrospinning of Continuous and Scalable Multifunctional MXene-Infiltrated Nanoyarns. *Small* **2020**, *16*, 2002158. [CrossRef]
61. Ajnsztajn, A.; Ferguson, S.; Thostenson, J.O.; Ngaboyamahina, E.; Parker, C.B.; Glass, J.T.; Stiff-Roberts, A.D. Transparent MXene-Polymer Supercapacitive Film Deposited Using RIR-MAPLE. *Crystals* **2020**, *10*, 152. [CrossRef]
62. Yun, T.; Kim, H.; Iqbal, A.; Cho, Y.S.; Lee, G.S.; Kim, M.K.; Kim, S.J.; Kim, D.; Gogotsi, Y.; Kim, S.O.; et al. Electromagnetic Shielding of Monolayer MXene Assemblies. *Adv. Mater.* **2020**, *32*, 1906769. [CrossRef]
63. Zhou, B.; Su, M.J.; Yang, D.Z.; Han, G.J.; Feng, Y.Z.; Wang, B.; Ma, J.L.; Ma, J.M.; Liu, C.T.; Shen, C.Y. Flexible MXene/Silver Nanowire-Based Transparent Conductive Film with Electromagnetic Interference Shielding and Electro-Photo-Thermal Performance. *ACS Appl. Mater. Interfaces* **2020**, *12*, 40859–40869. [CrossRef]
64. Wan, Y.Z.; Xiong, P.X.; Liu, J.Z.; Feng, F.F.; Xun, X.W.; Gama, F.M.; Zhang, Q.C.; Yao, F.L.; Yang, Z.W.; Luo, H.L.; et al. Ultrathin, Strong, and Highly Flexible $Ti_3C_2T_x$ MXene/Bacterial Cellulose Composite Films for High-Performance Electromagnetic Interference Shielding. *ACS Nano* **2021**, *15*, 8439–8449. [CrossRef]
65. Li, E.; Pan, Y.M.; Wang, C.F.; Liu, C.T.; Shen, C.Y.; Pan, C.F.; Liu, X.H. Multifunctional and superhydrophobic cellulose composite paper for electromagnetic shielding, hydraulic triboelectric nanogenerator and Joule heating applications. *Chem. Eng. J.* **2021**, *420*, 129864. [CrossRef]
66. Wang, X.F.; Lei, Z.W.; Ma, X.D.; He, G.F.; Xu, T.; Tan, J.; Wang, L.L.; Zhang, X.S.; Qu, L.J.; Zhang, X.J. A lightweight MXene-Coated nonwoven fabric with excellent flame Retardancy, EMI Shielding, and Electrothermal/Photothermal conversion for wearable heater. *Chem. Eng. J.* **2022**, *430*, 132605. [CrossRef]
67. Han, M.K.; Shuck, C.E.; Rakhmanov, R.; Parchment, D.; Anasori, B.; Koo, C.M.; Friedman, G.; Gogotsi, Y. Beyond $Ti_3C_2T_x$: MXenes for Electromagnetic Interference Shielding. *ACS Nano* **2020**, *14*, 5008–5016. [CrossRef]
68. Li, G.H.; Wyatt, B.C.; Song, F.; Yu, C.Q.; Wu, Z.J.; Xie, X.Q.; Anasori, B.; Zhang, N. 2D Titanium Carbide (MXene) Based Films: Expanding the Frontier of Functional Film Materials. *Adv. Funct. Mater.* **2021**, *31*, 2105043. [CrossRef]
69. Cao, W.T.; Ma, C.; Tan, S.; Ma, M.G.; Wan, P.B.; Chen, F. Ultrathin and Flexible CNTs/MXene/Cellulose Nanofibrils Composite Paper for Electromagnetic Interference Shielding. *Nano-Micro Lett.* **2019**, *11*, 72. [CrossRef]

70. Wan, S.J.; Li, X.; Chen, Y.; Liu, N.N.; Du, Y.; Dou, S.X.; Jiang, L.; Cheng, Q.F. High-strength scalable MXene films through bridging-induced densification. *Science* **2021**, *374*, 96–99. [CrossRef]
71. Wang, J.F.; He, J.B.; Kan, D.X.; Chen, K.Y.; Song, M.S.; Huo, W.T. MXene Film Prepared by Vacuum-Assisted Filtration: Properties and Applications. *Crystals* **2022**, *12*, 1034. [CrossRef]
72. Tang, T.T.; Wang, S.C.; Jiang, Y.; Xu, Z.G.; Chen, Y.; Peng, T.S.; Khan, F.; Feng, J.B.; Song, P.G.; Zhao, Y. Flexible and flame-retarding phosphorylated MXene/polypropylene composites for efficient electromagnetic interference shielding. *J. Mater. Sci. Technol.* **2022**, *111*, 66–75. [CrossRef]
73. Jin, X.X.; Wang, J.F.; Dai, L.Z.; Liu, X.Y.; Li, L.; Yang, Y.Y.; Cao, Y.X.; Wang, W.J.; Wu, H.; Guo, S.Y. Flame-retardant poly(vinyl alcohol)/MXene multilayered films with outstanding electromagnetic interference shielding and thermal conductive performances. *Chem. Eng. J.* **2020**, *380*, 122475. [CrossRef]
74. Wang, Q.W.; Zhang, H.B.; Liu, J.; Zhao, S.; Xie, X.; Liu, L.X.; Yang, R.; Koratkar, N.; Yu, Z.Z. Multifunctional and Water-Resistant MXene-Decorated Polyester Textiles with Outstanding Electromagnetic Interference Shielding and Joule Heating Performances. *Adv. Funct. Mater.* **2019**, *29*, 1806819. [CrossRef]
75. Luo, J.M.; Zhang, W.K.; Yuan, H.D.; Jin, C.B.; Zhang, L.Y.; Huang, H.; Liang, C.; Xia, Y.; Zhang, J.; Gan, Y.P.; et al. Pillared Structure Design of MXene with Ultralarge Interlayer Spacing for High-Performance Lithium-Ion Capacitors. *ACS Nano* **2017**, *11*, 2459–2469. [CrossRef]
76. Zou, Z.; Ning, M.Q.; Lei, Z.K.; Zhuang, X.H.; Tan, G.G.; Hou, J.H.; Xu, H.; Man, Q.K.; Li, J.B.; Li, R.W. 0D/1D/2D architectural Co@C/MXene composite for boosting microwave attenuation performance in 2-18 GHz. *Carbon* **2022**, *193*, 182–194. [CrossRef]
77. Li, X.; You, W.B.; Xu, C.Y.; Wang, L.; Yang, L.T.; Li, Y.S.; Che, R.C. 3D Seed-Germination-Like MXene with In Situ Growing CNTs/Ni Heterojunction for Enhanced Microwave Absorption via Polarization and Magnetization. *Nano-Micro Lett.* **2021**, *13*, 157. [CrossRef]
78. Zong, Z.; Ren, P.G.; Guo, Z.Z.; Wang, J.; Chen, Z.Y.; Jin, Y.L.; Ren, F. Three-dimensional macroporous hybrid carbon aerogel with heterogeneous structure derived from MXene/cellulose aerogel for absorption-dominant electromagnetic interference shielding and excellent thermal insulation performance. *J. Colloid Interface Sci.* **2022**, *619*, 96–105. [CrossRef]
79. Wang, L.; Song, P.; Lin, C.T.; Kong, J.; Gu, J.W. 3D Shapeable, Superior Electrically Conductive Cellulose Nanofibers/$Ti_3C_2T_x$ MXene Aerogels/Epoxy Nanocomposites for Promising EMI Shielding. *Research* **2020**, *2020*, 4093732. [CrossRef]
80. Fan, Z.M.; Wang, D.L.; Yuan, Y.; Wang, Y.S.; Cheng, Z.J.; Liu, Y.Y.; Xie, Z.M. A lightweight and conductive MXene/graphene hybrid foam for superior electromagnetic interference shielding. *Chem. Eng. J.* **2020**, *381*, 122696. [CrossRef]
81. Wang, H.Y.; Sun, X.B.; Xin, Y.; Yang, S.H.; Hu, P.F.; Wang, G.S. Ultrathin self-assembly MXene/Co-based bimetallic oxide heterostructures as superior and modulated microwave absorber. *J. Mater. Sci. Technol.* **2023**, *134*, 132–141. [CrossRef]
82. Wang, H.Y.; Sun, X.B.; Yang, S.H.; Zhao, P.Y.; Zhang, X.J.; Wang, G.S.; Huang, Y. 3D Ultralight Hollow NiCo Compound@MXene Composites for Tunable and High-Efficient Microwave Absorption. *Nano-Micro Lett.* **2021**, *13*, 206. [CrossRef]
83. Niu, H.H.; Tu, X.Y.; Zhang, S.; Li, Y.Y.; Wang, H.L.; Shao, G.; Zhang, R.; Li, H.X.; Zhao, B.; Fan, B.B. Engineered core-shell SiO_2@$Ti_3C_2T_x$ composites: Towards ultra-thin electromagnetic wave absorption materials. *Chem. Eng. J.* **2022**, *446*, 137260. [CrossRef]
84. Chen, F.; Zhang, S.S.; Ma, B.B.; Xiong, Y.; Luo, H.; Cheng, Y.Z.; Li, X.C.; Wang, X.; Gong, R.Z. Bimetallic CoFe-MOF@$Ti_3C_2T_x$ MXene derived composites for broadband microwave absorption. *Chem. Eng. J.* **2022**, *431*, 134007. [CrossRef]
85. Li, Y.; Meng, F.B.; Mei, Y.; Wang, H.G.; Guo, Y.F.; Wang, Y.; Peng, F.X.; Huang, F.; Zhou, Z.W. Electrospun generation of $Ti_3C_2T_x$ MXene@graphene oxide hybrid aerogel microspheres for tunable high-performance microwave absorption. *Chem. Eng. J.* **2020**, *391*, 123512. [CrossRef]
86. Wang, Y.Q.; Zhao, H.B.; Cheng, J.B.; Liu, B.W.; Fu, Q.; Wang, Y.Z. Hierarchical $Ti_3C_2T_x$@ZnO Hollow Spheres with Excellent Microwave Absorption Inspired by the Visual Phenomenon of Eyeless Urchins. *Nano-Micro Lett.* **2022**, *14*, 76. [CrossRef]
87. Cui, Y.H.; Yang, K.; Wang, J.Q.; Shah, T.; Zhang, Q.Y.; Zhang, B.L. Preparation of pleated RGO/MXene/Fe_3O_4 microsphere and its absorption properties for electromagnetic wave. *Carbon* **2021**, *172*, 1–14. [CrossRef]
88. Wu, F.; Liu, Z.H.; Wang, J.Q.; Shah, T.; Liu, P.; Zhang, Q.Y.; Zhang, B.L. Template-free self-assembly of MXene and CoNi-bimetal MOF into intertwined one-dimensional heterostructure and its microwave absorbing properties. *Chem. Eng. J.* **2021**, *422*, 130591. [CrossRef]
89. Li, X.; Wu, Z.C.; You, W.B.; Yang, L.T.; Che, R.C. Self-Assembly MXene-rGO/CoNi Film with Massive Continuous Heterointerfaces and Enhanced Magnetic Coupling for Superior Microwave Absorber. *Nano-Micro Lett.* **2022**, *14*, 73. [CrossRef]
90. Hu, K.X.; Wang, H.H.; Zhang, X.; Huang, H.; Qiu, T.; Wang, Y.; Zhang, C.F.; Pan, L.M.; Yang, J. Ultralight $Ti_3C_2T_x$ MXene foam with superior microwave absorption performance. *Chem. Eng. J.* **2021**, *408*, 127283. [CrossRef]
91. Jia, X.C.; Shen, B.; Zhang, L.H.; Zheng, W.G. Construction of compressible Polymer/MXene composite foams for high-performance absorption-dominated electromagnetic shielding with ultra-low reflectivity. *Carbon* **2021**, *173*, 932–940. [CrossRef]
92. Zhang, Y.; Xu, M.K.; Wang, Z.G.; Zhao, T.Y.; Liu, L.X.; Zhang, H.B.; Yu, Z.Z. Strong and conductive reduced graphene oxide-MXene porous films for efficient electromagnetic interference shielding. *Nano Res.* **2022**, *15*, 4916–4924. [CrossRef]
93. Liu, L.; Ma, Z.W.; Zhu, M.H.; Liu, L.N.; Dai, J.F.; Shi, Y.Q.; Gao, J.F.; Dinh, T.; Nguyen, T.; Tang, L.C.; et al. Superhydrophobic self-extinguishing cotton fabrics for electromagnetic interference shielding and human motion detection. *J. Mater. Sci. Technol.* **2023**, *132*, 59–68. [CrossRef]
94. Zhang, Y.L.; Ruan, K.P.; Gu, J.W. Flexible Sandwich-Structured Electromagnetic Interference Shielding Nanocomposite Films with Excellent Thermal Conductivities. *Small* **2021**, *17*, 2101951. [CrossRef]

95. Chen, W.; Liu, L.X.; Zhang, H.B.; Yu, Z.Z. Flexible, Transparent, and Conductive $Ti_3C_2T_x$ MXene-Silver Nanowire Films with Smart Acoustic Sensitivity for High-Performance Electromagnetic Interference Shielding. *ACS Nano* **2020**, *14*, 16643–16653. [CrossRef]
96. Wang, J.; Ma, X.Y.; Zhou, J.L.; Du, F.L.; Teng, C. Bioinspired, High-Strength, and Flexible MXene/Aramid Fiber for Electromagnetic Interference Shielding Papers with Joule Heating Performance. *ACS Nano* **2022**, *16*, 6700–6711. [CrossRef]
97. Zhang, D.B.; Yin, R.; Zheng, Y.J.; Li, Q.M.; Liu, H.; Liu, C.T.; Shen, C.Y. Multifunctional MXene/CNTs based flexible electronic textile with excellent strain sensing, electromagnetic interference shielding and Joule heating performances. *Chem. Eng. J.* **2022**, *438*, 135587. [CrossRef]
98. Wang, Y.; Qi, Q.B.; Fan, J.; Wang, W.; Yu, D. Simple and robust MXene/carbon nanotubes/cotton fabrics for textile wastewater purification via solar-driven interfacial water evaporation. *Sep. Purif. Technol.* **2021**, *254*, 117615. [CrossRef]
99. Li, R.Y.; Zhang, L.B.; Shi, L.; Wang, P. MXene Ti_3C_2: An Effective 2D Light-to-Heat Conversion Material. *ACS Nano* **2017**, *11*, 3752–3759. [CrossRef]
100. Lin, H.; Wang, X.G.; Yu, L.D.; Chen, Y.; Shi, J.L. Two-Dimensional Ultrathin MXene Ceramic Nanosheets for Photothermal Conversion. *Nano Lett.* **2017**, *17*, 384–391. [CrossRef]
101. Zhang, X.S.; Wang, X.F.; Lei, Z.W.; Wang, L.L.; Tian, M.W.; Zhu, S.F.; Xiao, H.; Tang, X.N.; Qu, L.J. Flexible MXene-Decorated Fabric with Interwoven Conductive Networks for Integrated Joule Heating, Electromagnetic Interference Shielding, and Strain Sensing Performances. *ACS Appl. Mater. Interfaces* **2020**, *12*, 14459–14467. [CrossRef]
102. Zhang, Y.; Gao, Q.; Zhang, S.; Fan, X.; Qin, J.B.; Shi, X.T.; Zhang, G.C. rGO/MXene sandwich-structured film at spunlace non-woven fabric substrate: Application to EMI shielding and electrical heating. *J. Colloid Interface Sci.* **2022**, *614*, 194–204. [CrossRef]
103. Jia, P.F.; Zhu, Y.L.; Lu, J.Y.; Wang, B.Y.; Song, L.; Wang, B.B.; Hu, Y. Multifunctional fireproof electromagnetic shielding polyurethane films with thermal management performance. *Chem. Eng. J.* **2022**, *439*, 135673. [CrossRef]
104. Cheng, H.R.; Xing, L.L.; Zuo, Y.; Pan, Y.M.; Huang, M.N.; Alhadhrami, A.; Ibrahim, M.M.; El-Bahy, Z.M.; Liu, C.T.; Shen, C.Y.; et al. Constructing nickel chain/MXene networks in melamine foam towards phase change materials for thermal energy management and absorption-dominated electromagnetic interference shielding. *Adv. Compos. Hybrid Mater.* **2022**, *5*, 755–765. [CrossRef]
105. Cheng, H.R.; Pan, Y.M.; Wang, X.; Liu, C.T.; Shen, C.Y.; Schubert, D.W.; Guo, Z.H.; Liu, X.H. Ni Flower/MXene-Melamine Foam Derived 3D Magnetic/Conductive Networks for Ultra-Efficient Microwave Absorption and Infrared Stealth. *Nano-Micro Lett.* **2022**, *14*, 63. [CrossRef]
106. Wang, S.J.; Li, D.S.; Zhou, Y.; Jiang, L. Hierarchical $Ti_3C_2T_x$ MXene/Ni Chain/ZnO Array Hybrid Nanostructures on Cotton Fabric for Durable Self-Cleaning and Enhanced Microwave Absorption. *ACS Nano* **2020**, *14*, 8634–8645. [CrossRef]
107. Zhu, M.; Yan, X.X.; Xu, H.L.; Xu, Y.J.; Kong, L. Ultralight, compressible, and anisotropic MXene@Wood nanocomposite aerogel with excellent electromagnetic wave shielding and absorbing properties at different directions. *Carbon* **2021**, *182*, 806–814. [CrossRef]
108. Lu, Z.Q.; Jia, F.F.; Zhuo, L.H.; Ning, D.D.; Gao, K.; Xie, F. Micro-porous MXene/Aramid nanofibers hybrid aerogel with reversible compression and efficient EMI shielding performance. *Compos. Part B Eng.* **2021**, *217*, 108853. [CrossRef]
109. Du, Y.Q.; Xu, J.; Fang, J.Y.; Zhang, Y.T.; Liu, X.Y.; Zuo, P.Y.; Zhuang, Q.X. Ultralight, highly compressible, thermally stable MXene/aramid nanofiber anisotropic aerogels for electromagnetic interference shielding. *J. Mater. Chem. A* **2022**, *10*, 6690–6700. [CrossRef]
110. Nguyen, V.T.; Min, B.K.; Yi, Y.; Kim, S.J.; Choi, C.G. MXene($Ti_3C_2T_x$)/graphene/PDMS composites for multifunctional broadband electromagnetic interference shielding skins. *Chem. Eng. J.* **2020**, *393*, 124608. [CrossRef]

Disclaimer/Publisher's Note: The statements, opinions and data contained in all publications are solely those of the individual author(s) and contributor(s) and not of MDPI and/or the editor(s). MDPI and/or the editor(s) disclaim responsibility for any injury to people or property resulting from any ideas, methods, instructions or products referred to in the content.